Received: 16 March 2023 | Revised: 8 July 2023 | Accepted: 25 July 2023
DOI: 10.1002/mma.9607

RESEARCH ARTICLE

WILEY

Hydrodynamics simulation of red blood cells: Employing a penalty method with double jump composition of lower order time integrator

Aymen Laadhari[1] | **Ahmad Deeb**[1] | **Badr Kaoui**[2]

[1]Department of Mathematics, College of Arts and Sciences, Khalifa University, Abu Dhabi, United Arab Emirates

[2]Biomechanics and Bioengineering Laboratory (UMR 7338), CNRS and Université de Technologie de Compiègne, Centre de Rechreches de Royallieu, Compiègne, France

Correspondence
Aymen Laadhari, Department of Mathematics, College of Arts and Sciences, Khalifa University, Abu Dhabi, United Arab Emirates.
Email: Aymen.Laadhari@ku.ac.ae

Communicated by: D. Zeidan

Funding information
Khalifa University of Science and Technology, Grant/Award Number: FSU-2021-027 (#8474000367)

We propose a numerical framework tailored for simulating the dynamics of vesicles with inextensible membranes, which mimic red blood cells, immersed in a non-Newtonian fluid environment. A penalty method is proposed to handle the inextensibility constraint by relaxation, allowing a simple computer implementation and an affordable computational load compared to the full mixed formulation. To handle the high-order derivatives in the stress jump across the membrane, which arise due to the high geometric order of the Helfrich functional, we employ higher degree finite elements for spatial discretization. The time integration scheme relies on the double composition of the Crank–Nicolson scheme to achieve faster fourth-order convergence behavior. Additionally, an adaptive time-stepping strategy based on a third-order temporal integration error estimation is implemented. We address the main features of the proposed method, which is benchmarked against existing numerical and experimental results. Furthermore, we investigate the influence of non-Newtonian rheology on the system dynamics.

KEYWORDS
finite element method, flow composition, generalized newtonian model, Helfrich energy functional, projection on the real axis, red blood cell

MSC CLASSIFICATION
65Mxx, 65Nxx, 65L04, 65N30, 76M10

1 | INTRODUCTION

Prompted by their biomedical and therapeutic applications, the development of theoretical, experimental, and computational tools for a better understanding of the functioning processes of red blood cells (RBCs) has aroused great interest in the fields of biology [1], physics [2], mathematics [3], and scientific computing [4].

Blood, unlike ordinary fluids, is a complex biological fluid with several puzzling and ubiquitous behaviors that depend mainly on the underlying individual and collective interaction of its main corpuscles, the RBCs, suspended in plasma. The main physiological function of RBCs is the systemic delivery of oxygen thanks to their remarkable ability to resist

---

hydrodynamic stresses and to deform considerably when passing through narrow capillaries. This complex behavior has a strong impact on the hemorheology on a global scale and gives blood a non-Newtonian rheology, particularly in the microcirculation, damaged vessels, or aneurysm sites [5]. While healthy blood can be assumed to be Newtonian in large arteries, non-Newtonian hemorheological properties (shear thinning, viscoelasticity, thixotropy, and yield stress) cannot be overlooked in the microcirculation [6–8]. The inherently non-trivial spatio-temporal behaviors of individual RBCs and biomembranes continue to pose a formidable challenge to numerical modeling [9–11]. Biomimetic giant unilamellar liposomes (or phospholipid vesicles) represent simplified and excellent instrumental models for studying and providing insight into the underlying mechanics of RBCs. They are artificial bilayer membranes made of many lipid and protein components, and devoid of submembranous cytoskeleton. Nowadays, vesicles play an important role in the expanding field of synthetic biology, for instance, for the delivery of drugs in the treatment of cancer [12, 13] and the production of biomolecules [14]. It is therefore unquestionably of some biological importance to better understand the effect of complex hemorheology on the behaviors of the vesicles [15–17]. The aim of our work is to present a finite element framework suitable for studying the dynamics of a vesicle in a non-Newtonian power-law flow.

The biomembrane mechanics allow the vesicle to resist strong hydrodynamic stresses and large deformations in flow, but also to exhibit remarkable dynamics and an astonishing variety of shapes. According to the well-known pioneering work of Helfrich in the 1970s [18], the intrinsic properties are due, above all, to the minimization under constraints of the membrane bending energy (or elasticity of curvature), referred to as Canham–Helfrich–Evans or Helfrich model for short [18–20]. The corresponding force involves calculations of second-order derivative of the curvature (which can be seen as a BiLaplacian of a surface characteristic field) and fourth-order derivative of the shape [21–23], yielding a numerically stiff problem and strong limitations on the time step. We also refer to a recent work on a generalized and more complex energy functional for an heterogeneous membrane model as a function of shape invariants [3].

Existing numerical strategies for tracking deformable interfaces can be roughly classified into two categories. While interface tracking techniques (or Lagrangian) require moving mesh nodes to track the moving interface, interface-capturing approaches (or Eulerian) [24] are usually formulated on fixed meshes (which does not prevent the mesh adaptation) while mesh elements do not adhere to the moving interface; the latter, however, introduce an additional advection equation into the global coupled system to describe implicitly the free interface. Lagragian approaches include, for example, the *classical finite element method* with a mesh adapting to membrane discretization [25], the *boundary element method* using a Green kernel for transforming viscous volume integrals into surface integrals [26, 27], and the *immersed boundary method* [15, 28]. Eulerian approaches include, among others, the *level set method* [3, 29–33], the *phase field approach* [34], and the *isogeometric phase field method* [35]. Other numerical approaches include the *parametric finite element method* [11, 36], the *interfacial spectral boundary element method* [37], the *isogeometric boundary integral method* [38], the *isogeometric coupled finite element method and boundary element method* [39], and the *lattice Boltzmann method* [28].

In this work, we opt for a level set method due to the large deformations of the flowing vesicle, requiring robust and regular remeshing tools to update the twisted meshes. The method is convenient for the calculation of the geometric parameters needed to assess the membrane force on the vesicle. Therefore, a surface source term appears in the time-dependent momentum equation and is driven by the minimization of the Helfrich energy. As these are high-order derivatives of curvature, specific treatments are necessary if standard finite elements are used. To reduce the numerical oscillations and errors due to multiple projections and Lagrange interpolations (for lower order polynomials [30]) and non-physical adjustments of the level set function (for global mass conservation purposes [40, 41]), while accurately assessing the membrane force, we use higher order polynomial approximations for finite element spatial discretization [33].

The strongly coupled fluid dynamics and membrane mechanics result in a nonlinear PDE system that is difficult to solve. The development of an appropriate computational algorithm depends on the decoupling strategies. Although staggered strategies are widely used in the literature due to their attractiveness in terms of implementation and computational cost, they suffer from instabilities leading to strong constraints on the time step and are limited to very small regimes of inertia (in the Stokes limit) [42]. On the contrary, strongly coupled strategies (monolithic or iterative) exhibit more stability but are less used due to their complexity and difficulty in computing the Jacobian [35, 40]. To solve the problem with a reasonable computational cost and allow a straightforward implementation using standard generalized Stokes solvers, we will relax the inextensibility constraint on velocity by a penalty approach, while being able to reproduce and draw conclusions related to cell behaviors in a non-Newtonian fluid. Moreover, we use a tightly coupled strategy to improve stability, that is, we perform sub-iterations until a sufficient tolerance is reached.

Although increasing the finite element order is effective for calculating the membrane force, the overall error would be dominated at some level by the temporal discretization order. To follow with an increase in the order of approximation in time, we will rely on the composition methods to raise the order of approximation of the time integration scheme [43, 44]. Several variations exist in the literature, for example, composing low-order methods with the same step size to increase stability of stiff problems [45, 46] and composing basic one-step methods with variable step sizes [47, 48]. A discussion of numerical integration and structure-preserving algorithms for some composition and multi-step methods can be found in Hairer and Hairer [49]. Additionally, we perform adaptive time stepping to capture some promoted vesicle dynamics with better efficiency, while allowing the use of large time steps when vesicle motion is slow. The step size will be based on an error estimate of the temporal approximation, set up to a predefined accuracy requirement. Higher order numerical approximations can be obtained using integrators based on divergent series resummation [50], which have been applied to large time dynamics problems [51], stiff problems [52], and diffusion equations within the framework of proper generalized decomposition [53].

Henceforth, a second-order Crank–Nicolson scheme, referred to as CN, will be used for the time discretization for accuracy and stability reasons [33]. Note that the second-order backward differentiation scheme (BDF) [40] requires two previous approximated solutions, which can deteriorate the second order if an abrupt change in the function holds. We also make comparisons with the backward Euler scheme, denoted BE, usually used for the vesicle problem [30].

1.1 | Outline

This article is organized as follows: Section 2 contains preliminary notations and describes the mathematical model used for the simulation of an individual vesicle in non-Newtonian fluid. Section 3 introduces variational formulations for both penalty and full mixed strategies. The discretization by finite elements in space is introduced in Section 4. In Section 5, we elaborate the time integration scheme and the adaptive time-stepping strategy. In Section 6, numerical experiments are conducted for the dynamics of a single vesicle under linear shear flow. A numerical study of the convergence and validations against existing results in the literature highlight the main features of the method. The conclusions and findings are summarized in Section 7.

2 | MATHEMATICAL MODEL

In this section, we give the equations governing the phospholipid bilayer model, the interface-capturing technique, and the fluid dynamics in the surrounding domain.

2.1 | Notations and membrane model

We consider the physiologically realistic membrane model of Helfrich, where bending is the main mode of deformation [18]. Consider the schematic representation in Figure 1. Let $T > 0$ be the time period and $\Lambda \in \mathbb{R}^2$ be a connected bounded Lipschitz domain with an outward normal $\boldsymbol{\nu}$ defined a.e. on $\partial\Lambda$. For all $t \in (0, T)$, $\Omega(t) \subset \Lambda$ is the inner domain of the vesicle (cytoplasm) with $\Gamma(t) = \partial\Omega(t)$ Lipschitz continuous and $\Gamma(t) \cap \partial\Lambda = \emptyset$. The outside domain $\Lambda \backslash \Omega(t)$ represents the plasma. Let us denote by H and K the mean and Gauss curvatures, corresponding, respectively, to the sum and the product of the principal curvatures on Γ. Helfrich introduced a model in which the membrane's mechanical deformations are monitored by the minimization of a scalar stored energy of high geometrical order. The latter depends on the squared L2 norm of the difference between the mean curvature and a curvature characteristic of the compositions of non-symmetrical membranes:

$$\mathsf{J}(\Omega) = \frac{k_b}{2} \int_{\partial\Omega} (H(\Omega) - H_0)^2 \, d\boldsymbol{s} + k_g \int_{\partial\Omega} K(\Omega) \, d\boldsymbol{s}, \tag{2.1}$$

where $k_b \approx 10^{-20}/10^{-19}$ kg m^2 s^{-2} represents the bending rigidity modulus [54] and k_g is the saddle splay modulus [55]. The energy is reduced to the Willmore energy when $H_0 = 0$ [56]. Based on the Gauss–Bonnet theorem, the term weighted by k_g can be neglected since it is invariant within a fixed topology class and constant Gaussian bending rigidity [57]. The spontaneous curvature H_0 allows to describe a possible asymmetry of the membrane at rest, which can be generated by the presence of different chemical properties in the internal and external subdomains of the vesicle. In this work, we set $H_0 = 0$ since this parameter is only relevant in 3D [35]. The minimization of the bending energy provides high-order nonlinear force and numerically stiff problem with stringent time-step limitations.

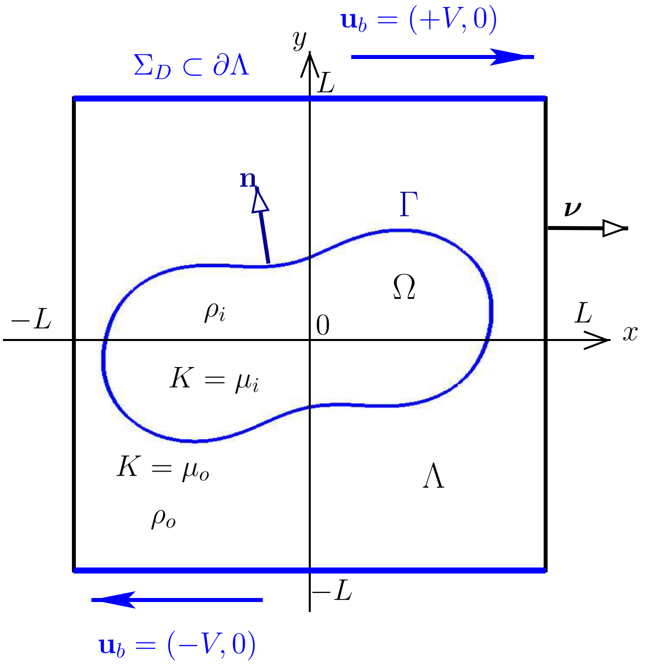

FIGURE 1 Sketch for the two-dimensional the studied numerical setup of a vesicle imbedded into a square domain Λ under simple shear flow conditions. The domain Ω contains the inner fluid enclosed by the vesicle Γ. [Colour figure can be viewed at wileyonlinelibrary.com]

Since the bilayer thickness ($\approx$ 5 nm) is negligible compared to the vesicle size ($\approx$ 10 μm), the membrane can be treated as a two-dimensional surface embedded in 3D space. We introduce the following surface operators along the two-dimensional surface (or one-dimensional perimeter in 2D space) of the vesicle: the surface gradient $\boldsymbol{\nabla}_s$, the surface divergence div_s, and the surface Laplacian Δ_s [58]. Let us denote by $\mathbf{I}$ the identity tensor, $\otimes$ the tensorial product, and $:$ the two times contracted tensor product. Given a regular and orientable surface $\Gamma \subset \mathbb{R}^2$ and its outward pointing normal vector $\mathbf{n}$, we employ the shorthand notation $\boldsymbol{\pi}_\Gamma = \mathbf{I} - \mathbf{n} \otimes \mathbf{n}$ for the surface unit tensor on Γ. Consider sufficiently smooth scalar-valued function q and $\mathbb{R}^d$-valued function $\boldsymbol{\nu}$ functions, with $d = 1, 2$. The surface operators write

$$\begin{aligned}\underset{s}{\boldsymbol{\nabla}} q &\equiv \boldsymbol{\pi}_\Gamma \, \boldsymbol{\nabla} q = \boldsymbol{\nabla} q - (\mathbf{n} \cdot \boldsymbol{\nabla} q)\mathbf{n},\\ div_s \boldsymbol{\nu} &\equiv \mathrm{tr}(\underset{s}{\boldsymbol{\nabla}} \boldsymbol{\nu}) = \boldsymbol{\pi}_\Gamma : \boldsymbol{\nabla} \boldsymbol{\nu},\\ \Delta_s q &\equiv div_s \underset{s}{\boldsymbol{\nabla}} q.\end{aligned}$$

Using shape derivation tools [21, 22], the bending Helfrich force can be expressed in the two-dimensional case as

$$\boldsymbol{F}_\Gamma = k_b \left(\Delta_s H + \frac{H^3}{2} \right) \mathbf{n}, \quad \text{on} \quad (0, T) \times \Gamma.$$

The balance of surface forces and hydrodynamic stresses acting on the membrane allows the fluid–membrane coupling through the jump of the normal Cauchy stress (2.3f) [40, 59]. Hence, the force $\boldsymbol{F}_\Gamma$ can be written as a forcing term acting locally on the membrane in the right side of the momentum equation. The mean curvature writes $H = \mathrm{div}_s \mathbf{n}$, while K degenerates in the two-dimensional case [60].

Furthermore, the vesicle's mechanics is subject to specific constraints requiring a close look at the biological properties of vesicles. In fact, the membrane structure comprises amphiphilic phospholipids having a hydrophilic head and hydrophobic tails. This phospholipid bilayer is impermeable (i.e., there is no osmosis), and the number of molecules remains fixed in each layer. As a result, the energy cost of stretching the vesicle membrane is too great compared to the cost of bending deformations. Therefore, all deformations are constrained to the local membrane inextensibility that forces the velocity surface divergence to vanish on the membrane; this in-plane fluid-like behavior of biomembranes, which resist stretching (but not shearing), results in the conservation of the global vesicle's perimeter (or area in 3D); see the discussion by Helfrich et al. [55]. This constraint is most often imposed either (i) by a local Lagrange multiplier taking the sense of position-dependent tension along the membrane which can be seen as a localized surface pressure [40] or (ii) by a local elastic force depending on the stretching of the membrane which can be quantified by the gradient of the level set function [29]. The latter approach has its practical advantages but does not allow exact imposition of the inextensibility constraint and introduces an additional highly nonlinear elastic force on the membrane; numerical stability can also be challenging.

In addition, phospholipid vesicles represent a form of biological barrier where material exchange is minimal between closed and surrounding compartments. We assume the incompressibility in the inner and outer fluid subdomains $\Omega(t)$ and $\Lambda\backslash\Omega(t)$. The membrane thus evolves with conserved area and enclosed volume.

2.2 | Level set framework

Consider an implicit representation of the membrane $\Gamma(t) = \{(t, \boldsymbol{x}) \in (0,T)\times\Lambda \, \text{s.t.}\, \varphi(t,\boldsymbol{x}) = 0\}$, which is described as an isosurface zero of the level set function φ in the embedding space Λ. Let $\boldsymbol{u}$ be the velocity vector. Initialized by a signed distance φ_0, the level set obeys a Hamilton–Jacobi equation (2.3a):

$$\frac{\partial\varphi}{\partial t} + \boldsymbol{u}\cdot\boldsymbol{\nabla}\varphi = 0, \text{ in } (0,T)\times\Lambda,$$

with a boundary condition $\varphi = \varphi_b$ on the upstream boundary $\Sigma_-(t) = \{\boldsymbol{x} \in \partial\Lambda \, \text{s.t.}\, \boldsymbol{u}(t,\boldsymbol{x})\cdot\boldsymbol{\nu}(\boldsymbol{x}) < 0\}$ [24, 60–63]. The geometrical information about the membrane such as the outward unit normal $\mathbf{n} = \boldsymbol{\nabla}\varphi/|\boldsymbol{\nabla}\varphi|$, mean curvature H, bending force $\boldsymbol{F}_\Gamma$, and surface operators are all encoded in a natural way in terms of φ. They are consequently extended to the entire domain Λ. The signed distance property is not preserved over time by the transport of the level set, inducing numerical instabilities due to large or small level set gradients. A redistancing problem is solved on a regular basis [62].

In an Eulerian framework, surface integrals are approximated as integrals over the whole Λ. Consider $\varepsilon > 0$ a small regularization parameter proportional to the size of the local mesh; it characterizes the width of the transition layer. Given a function η defined on Γ and its extension $\tilde{\eta}$ to Λ, the smoothed one-dimensional Heaviside $\mathcal{H}_\varepsilon$ and Dirac δ_ε functions

$$\mathcal{H}_\varepsilon(\varphi) = \begin{cases} 0, & \text{when } \varphi < -\varepsilon \\ \frac{1}{2}\left(1 + \frac{\varphi}{}\varepsilon + \frac{1}{\pi}\sin\left(\frac{\pi\varphi}{\varepsilon}\right)\right), & \text{when } |\varphi| \leqslant \varepsilon, \\ 1, & \text{otherwise} \end{cases} \quad \text{and} \quad \delta_\varepsilon(\varphi) = \frac{\mathrm{d}\mathcal{H}_\varepsilon}{\mathrm{d}\varphi}(\varphi)$$

allow easy approximations of surface integrals as bulk integrals:

$$\int_\Gamma \eta(\boldsymbol{x})\, d\boldsymbol{s} \approx \int_\Lambda |\nabla\varphi|\, \delta_\varepsilon(\varphi)\, \tilde{\eta}(\boldsymbol{x})\, \mathrm{d}\boldsymbol{x}. \tag{2.2}$$

2.3 | Continuous setting of the coupled nonlinear problem

Let $\boldsymbol{u}$, p, and $\mathbf{I}$ be the fluid velocity, pressure, and identity tensor, respectively. Unlike Newtonian constitutive model characterized by a linear stress-strain relationship, the vesicle is suspended in an incompressible non-Newtonian fluid, where the constitutive law expresses the Cauchy stress as follows:

$$\boldsymbol{\sigma} = 2\eta\left(|2\mathbf{Du}|^2\right)\mathbf{Du} - p\mathbf{I}, \text{ with a shear strain rate tensor } \mathbf{Du} = \frac{\boldsymbol{\nabla}\boldsymbol{u} + \boldsymbol{\nabla}\boldsymbol{u}^T}{2}.$$

Here, $|\boldsymbol{\tau}| = \left(\frac{1}{2}\boldsymbol{\tau} : \boldsymbol{\tau}\right)^{1/2}$, with $\boldsymbol{\tau} \in \mathbb{R}^{3\times 3}$, denotes the conventional tensor norm. It follows that $|2\mathbf{Du}|^2 = 2\mathbf{Du} : \mathbf{Du}$. We consider an empirically measured shear-rate-dependent blood viscosity that follows a power law:

$$\eta(\gamma) = K\gamma^{(\varsigma-1)/2}, \text{ with } \gamma \in \mathbb{R}^+.$$

The stress power-law index $\varsigma = 0.7755 < 1$ characterizes a physiological shear thinning behavior of blood and is obtained by multiple regressions on blood viscometric data. That is, the viscosity exponentially decreases with increasing shear rates. We assume constant piecewise consistency index $K = \mu_i$ and $K = \mu_o$ in Ω and $\Lambda\backslash\Omega$, respectively, which coincide with the constant viscosities in the inner and and outer fluid domains in the Newtonian case $\varsigma = 1$. Constant densities ρ_i and ρ_o are considered in the intra- and extra-membrane regions. The density is then defined as a regularized function $\rho_\varepsilon(\varphi) = \rho_o \mathcal{H}_\varepsilon(\varphi) + \rho_i (1 - \mathcal{H}_\varepsilon(\varphi))$, which allow the use of non-conforming meshes.

Consider a vesicle under linear shear flow in a square domain of size $2L$; see Figure 1. A no-slip condition $\boldsymbol{u} = (\pm V, 0)$ is prescribed on the horizontal boundaries Σ_D which moves with opposite constant velocity, while stress-free conditions are imposed elsewhere on $\Sigma_N = \partial\Lambda \backslash \Sigma_D$. Dirichlet boundary conditions are imposed for φ on the upstream boundary Σ_-. Therefore, the space of velocity fields can be written as

$$\mathbb{V}(\mathbf{u}_b) = \left\{ \mathbf{v} \in \left(H^1(\Lambda)\right)^2 \text{s.t.} \mathbf{v} = \mathbf{u}_b \ \text{ on } \ \Sigma_D \right\}.$$

Let $|\Gamma|$ and $|\Omega|$ be the perimeter and the area of the internal domain, respectively. To normalize the equations, we choose the length scale $R = |\Gamma|/2\pi$ describing the typical size of the vesicle, the velocity scale $U = VR/L$, the pressure unit $\mu_o U/R$, and the time unit R/U. That results three dimensionless physical parameters: the Reynolds number Re, the bending capillary number Bn, and the viscosity contrast β, which are completed by two geometrical parameters: the reduced area Ξ_{2D} and the confinement level γ.

$$\text{Re} = \frac{\rho_o U R}{\mu_o}, \ \text{Bn} = \frac{\mu_o R^2 U}{k_b}, \ \beta = \frac{\mu_i}{\mu_o}, \ \Xi_{2D} = \frac{|\Omega|/\pi}{(|\Gamma|/2\pi)^2}, \ \text{ and } \ \gamma = \frac{R}{L}.$$

The Reynolds number compares the inertial effect of the fluid to the viscous forces, while the bending number compares the force of the imposed flow to the resistance of the membrane to bending. The reduced area Ξ_{2D} compares the area of the internal domain bounded by the vesicle with that of a circle having the same perimeter as the vesicle. It reaches its maximum value $\Xi_{2D} = 1$ for a circle. At the RBCs scale, blood inertia is negligibly small, and the dynamics is dominated by the viscous forces, with low Reynolds typically in the order of 10^{-3} or less [64]. Note that, according to discussions in Laadhari et al. [65] and Salac and Miksis [66], higher Reynolds regimes (greater than 1) can be achieved in specific contexts, for example, in the case of stenosed vessels and of atherothrombosis. That is beyond the scope of this work.

The coupling and fluid–membrane interactions are incorporated by the Eulerian formalism. The regularized Cauchy stress tensor is thus a function of the dimensionless and smoothed viscosity function according to

$$2\mu_\varepsilon(\varphi)\,|2\mathbf{Du}|^{\varsigma-1} \equiv 2\left(\mathcal{H}_\varepsilon(\varphi) + \beta\,(1 - \mathcal{H}_\varepsilon(\varphi))\right)|2\mathbf{Du}|^{\varsigma-1}.$$

The constrained space of admissible velocities reads

$$\mathbb{K}(\mathbf{u}_b) = \{\mathbf{v} \in \mathbb{V}(\mathbf{u}_b) \text{s.t.} \operatorname{div}\, \mathbf{v} = 0 \ \text{ in } \ \Lambda \ \text{ and } \ \operatorname{div}_s \mathbf{v} = 0 \ \text{ on } \ \Gamma\}.$$

Assume the continuity of the fluid velocity at the membrane. Supplemented with suitable initial and boundary conditions, the nonlinear coupled problem describing the vesicle-hydrodynamic interactions is stated as

Find φ, $\boldsymbol{u}$, p, and λ such that

$$\frac{\partial \varphi}{\partial t} + \mathbf{u}.\boldsymbol{\nabla}\,\varphi = 0 \ \text{ in } \ (0, T) \times \Lambda, \tag{2.3a}$$

$$\text{Re}\left(\frac{\partial \mathbf{u}}{\partial t} + \mathbf{u}.\boldsymbol{\nabla}\,\mathbf{u}\right) - \mathbf{div}\left(2\mu_\varepsilon(\varphi)\,|2\mathbf{Du}|^{\varsigma-1}\,\mathbf{Du}\right) + \boldsymbol{\nabla}\,p = \boldsymbol{0} \ \text{ in } \ (0, T) \times (\Lambda \backslash \Gamma), \tag{2.3b}$$

$$-\operatorname{div}\ \mathbf{u} = 0 \ \text{ in } \ (0, T) \times \Lambda, \tag{2.3c}$$

$$-\operatorname{div}_s \mathbf{u} = 0 \ \text{ on } \ (0, T) \times \Gamma, \tag{2.3d}$$

$$[\mathbf{u}] = \boldsymbol{0} \ \text{ on } \ (0, T) \times \Gamma, \tag{2.3e}$$

$$-\frac{1}{\text{Bn}}\left\{\Delta_s H + \frac{H^3}{2}\right\}\mathbf{n} + H\,\lambda\,\mathbf{n} - \underset{s}{\boldsymbol{\nabla}}\lambda + \left[2\mu_\varepsilon(\varphi)\,|2\mathbf{Du}|^{\varsigma-1}\,\mathbf{Du} - p\boldsymbol{I}\right].\mathbf{n} = \boldsymbol{0} \ \text{ on } \ (0, T) \times \Gamma, \tag{2.3f}$$

$$\varphi = \varphi_b \text{ on } (0,T)\times\Sigma_-, \tag{2.3g}$$

$$\mathbf{u} = \mathbf{u}_b \text{ on } (0,T)\times\Sigma_D, \tag{2.3h}$$

$$\left(2\mu_\varepsilon(\varphi)\,|2\mathbf{Du}|^{\varsigma-1}\mathbf{Du} - p\boldsymbol{I}\right).\boldsymbol{\nu} = \boldsymbol{0} \text{ on } (0,T)\times\Sigma_N, \tag{2.3i}$$

$$\varphi(0) = \varphi_0 \text{ in } \Lambda, \tag{2.3j}$$

$$\mathbf{u}(0) = \mathbf{u}_0 \text{ in } \Lambda. \tag{2.3k}$$

Given a reduced area parameter, we initialize the vesicle as an ellipse in the horizontal position. Let $\boldsymbol{x} = (x, y) \in \Lambda$ be a spatial position. Hence, the shape of the vesicle is described through a level set function at t = 0 as follows:

$$\varphi_0(\boldsymbol{x}) = \frac{\sqrt{(x/\alpha)^2 + y^2/\left(2-\alpha^2\right)}}{\sqrt{\left(x/\alpha^2\right)^2 + y^2/\left(2-\alpha^2\right)^2}}\sqrt{(x/\alpha)^2 + \left(y/\left(2-\alpha^2\right)\right)^2} - R_0, \text{ with } R_0 = 0.45 \text{ and } \alpha = \sqrt{1+\sqrt{1-\Xi_{2D}}}.$$

The dynamics of the membrane is described at each time through the tilt angle $\theta(t) \in [-\pi/2, \pi/2]$ which forms with respect to the horizontal position. It can be obtained by the angle formed with the eigenvector associated with the largest eigenvalue of the matrix of inertia about the center of mass of the vesicle:

$$\boldsymbol{I}_\Gamma(t) = \int_{\Omega(t)}\left(\boldsymbol{x} - \frac{1}{|\Omega(t)|}\int_{\Omega(t)}\boldsymbol{x}\mathrm{d}\boldsymbol{x}\right)\otimes\left(\boldsymbol{x} - \frac{1}{|\Omega(t)|}\int_{\Omega(t)}\boldsymbol{x}\mathrm{d}\boldsymbol{x}\right)\mathrm{d}\boldsymbol{x}.$$

3 | VARIATIONAL FORMULATION AND PENALTY METHOD

We consider two strategies to address the inextensibility difficulty and enforce this constraint: either by using an exact Lagrange multiplier or by penalty. For the level set advection, we proceed with stabilization by introducing a stabilization bilinear form denoted by $S(\tau_K;\cdot,\cdot)$ depending on a local stabilization parameter denoted τ_K; see Section 4.

3.1 | Model A: Mixed velocity–pressure–tension formulation

Consider a spatially dependent Lagrange multiplier, referred to as λ, to enforce the local point-wise inextensibility constraint on the membrane. That is to say, the field λ acts in a small neighborhood of width 2ε around Γ and ensures the membrane tension necessary for inextensibility. It is extended, in a level set setting, to the entire domain Λ. While the curvature on the membrane can be calculated directly as the divergence of the normal vector, this calculation is problematic for Lagrange polynomials of lower degrees and can be a source of numerical instabilities [67]. In this work, we use high-order Lagrange polynomials instead of standard Lagrange finite elements with H^1 and C^0 regularity. We reduce the interpolation errors and projections between finite element spaces by introducing a mixed variable $\Psi = -\Delta_s H$, which will be evaluated based on a duality argument. Indeed, the surface Green formula on the closed surface Γ allows to compute Ψ in a weak sense, resulting in (3.1d).

Introducing the spaces of admissible fields $\boldsymbol{u}$, p, λ, and φ

$$\mathbb{V}(\boldsymbol{u}_b) = \left\{\boldsymbol{v} \in \left(H^1(\Lambda)\right)^2 \text{s.t.}\, \boldsymbol{v} = \boldsymbol{u}_b \text{ on } \Sigma_D\right\},\ L_0^2(\Lambda) = \left\{q \in L^2(\Lambda) \text{ s.t.} \int_\Omega q\,d\boldsymbol{x} = 0\right\},\ \mathbb{W} = \left\{\xi \in H^{-1/2}(\Gamma)\right\},$$
$$\mathbb{X} = \left\{\psi \in W^{1,\infty}(\Lambda) \cap H^1(\Lambda)\right\},\ \text{and } \mathbb{X}(\varphi_b) = \mathbb{X} \cap \left\{\psi \in L^\infty(\Lambda) \text{ s.t.}\, \psi = \varphi_b \text{ on } \Sigma_-\right\},$$

with a zero average constraint for the pressure space, the mixed variational formulation of the vesicle problem (2.3) writes

[**Model A**]: find $\boldsymbol{u} \in C^0\left((0,T),L^2(\Lambda)^d\right) \cap L^2\left((0,T),\mathbb{V}(\boldsymbol{u}_b)\right)$, $p \in L^2\left((0,T),L^2_0(\Lambda)\right)$, $\lambda \in L^2\left((0,T),\mathbb{W}\right)$ and $\varphi \in C^0\left((0,T),L^2(\Lambda)^d\right) \cap L^2\left((0,T),\mathbb{X}(\varphi_b)\right)$ such that

$$\begin{aligned}\mathrm{Re}\int\limits_{\Lambda}\left(\frac{\partial \boldsymbol{u}}{dt}+\boldsymbol{u}\cdot\nabla\boldsymbol{u}\right)\cdot\boldsymbol{v}+\int\limits_{\Lambda}2\left(\mathcal{H}_\varepsilon(\varphi)+\beta\left(1-\mathcal{H}_\varepsilon(\varphi)\right)\right)|2\mathbf{Du}|^{\varsigma-1}\,\mathbf{Du}:\mathbf{Dv}-\int\limits_{\Lambda}p\,div\boldsymbol{v}-\int\limits_{\Gamma}\lambda\,div_s\boldsymbol{v}&\\+\frac{1}{2\mathrm{Bn}}\int\limits_{\Gamma}\left(2\Psi-H^3\right)\mathbf{n}\cdot\boldsymbol{v}=\int\limits_{\Sigma_N}\boldsymbol{\sigma v}\cdot\boldsymbol{v},\qquad\qquad \forall\boldsymbol{v}\in\mathbb{V}(0),&\end{aligned}\tag{3.1a}$$

$$\int\limits_{\Lambda}q\,div\boldsymbol{u}=0,\qquad \forall q\in L^2_0(\Lambda),\tag{3.1b}$$

$$\int\limits_{\Gamma}\xi div_s\boldsymbol{u}=0,\qquad \forall\xi\in\mathbb{W},\tag{3.1c}$$

$$\int\limits_{\Gamma}\Psi\zeta+\int\limits_{\Gamma}\underset{s}{\boldsymbol{\nabla}}H\cdot\underset{s}{\boldsymbol{\nabla}}\zeta=0,\qquad \forall\zeta\in H^1(\Gamma),\tag{3.1d}$$

$$\int\limits_{\Lambda}\frac{\partial\varphi}{\partial t}\psi+\int\limits_{\Lambda}\left(\boldsymbol{u}\cdot\boldsymbol{\nabla}\varphi\right)\psi+\int\limits_{\Lambda}S\left(\tau_K;\varphi,\psi\right)=0,\qquad \forall\psi\in\mathbb{X}(0).\tag{3.1e}$$

3.2 | Model B: Penalty approach

We consider here a penalty approach to solve the vesicle problem with reasonable computational cost compared to the full mixed formulation involving the unknowns $\boldsymbol{u}$, p, and λ and also to allow a straightforward numerical implementation using standard generalized Stokes solvers usually available as a fundamental brick in all finite element libraries. The idea is to relax the surface divergence-free constraint (2.3d) in the variational formulation by a penalty term; it therefore follows that the inextensibility is not exactly fulfilled.

For the sake of simplicity, we present the penalty model in the case of the Stokes problem. With the term time derivative, the presentation is more technical and must consider the problem discretized in time using the method of characteristics to discretize the total derivative. We refer to Janela et al. [68] for a detailed presentation on modeling penalized rigid body motion. Let $K^*(t,x)$ be the dimensionless sharp function equal to β in $\Omega(t)$ and 1 otherwise. The vesicle problem (3.2) can be formulated as a minimization problem using an appropriate energy of dissipation function. Given any shape Ω and any admissible velocity $\boldsymbol{u}$ enough regular, the energy functional involves the Helfrich bending energy and the viscous energy, both depending on $\boldsymbol{u}$. Indeed, $\Gamma=\partial\Omega$ and H implicitly depend on $\mathbf{u}$ because they are encoded in terms of φ which is advected by $\boldsymbol{u}$. It is given by

$$J(\mathbf{u})=\frac{1}{\varsigma+1}\int\limits_{\Lambda}K^*\,|2\mathbf{Du}|^2\,d\boldsymbol{x}+\frac{1}{2\,\mathrm{Bn}}\int\limits_{\partial\Omega}H^2(\Omega)\,d\boldsymbol{s}.\tag{3.2}$$

The energy is minimized in the constrained space of incompressibility and inextensibility conditions:

$$\mathbf{u}=\underset{\mathbf{v}\in\mathbb{K}(t,\mathbf{u}_b)}{\arg\inf}J(\mathbf{v}).$$

The corresponding optimality system can be obtained by calculating the Gâteaux derivative. Let $H^{1/2}(\partial\Omega)$ be the space of the trace of elements of $H^1(\Omega)$ on $\partial\Omega$ [69]. The minimization problem is written as a saddle point problem:

$$(\mathbf{u}; p, \lambda) = \arg\inf_{\mathbf{v}\in\mathbb{V}(\mathbf{u}_b)} \sup_{\substack{q \in L^2(\Lambda) \\ \mu \in H^{1/2}(\partial\Omega)}} \left\{ J(\boldsymbol{v}) + \int_{\Lambda} q \operatorname{div}\boldsymbol{v}\, d\boldsymbol{x} + \int_{\partial\Omega} \mu \operatorname{div}_s \boldsymbol{v}\, d\boldsymbol{s} \right\}.$$

The variational optimality system results in the mixed formulation (3.1a) in case of zero Reynolds number, where p and λ two Lagrange multipliers to enforce the constraints in $\mathbb{K}(t, \mathbf{u}_b)$.

We introduce a penalty method to alleviate the inextensibility constraint in $\mathbb{K}(t, \mathbf{u}_b)$. Let ϵ be a small penalty coefficient, set equal to 10^{-7} in numerical calculations. We consider an unconstrained functional spaces with respect to the inextensibility for the velocities $\widetilde{\mathbb{K}}(t, \mathbf{u}_b)$:

$$\widetilde{\mathbb{K}}(t, \mathbf{u}_b) = \{\mathbf{v} \in \mathbb{V}(\mathbf{u}_b) \ s.t. \ \text{div } \mathbf{v} = 0 \ \text{ in } \ \Lambda\}.$$

The problem (3.2) will be approximated by the following minimization problem which penalizes the inextensibility constraint:

$$\boldsymbol{u}_\epsilon = \arg\inf_{\mathbf{v}\in\widetilde{\mathbb{K}}(t,\mathbf{u}_b)} J_\epsilon(\mathbf{v}).$$

The relaxed energy writes

$$J_\epsilon(\boldsymbol{u}) = J(\mathbf{u}) + \frac{1}{\epsilon} \int_{\partial\Omega} (div_s(\boldsymbol{u}))^2 \, d\boldsymbol{s}. \tag{3.3}$$

Similarly to the mixed formulation, the optimality system is derived after writing (3.2) as a saddle point problem, which is of practical interest for the finite element discretization. In the following, the explicit dependence of $\boldsymbol{u}_\epsilon$ and p_ϵ on ϵ will be understood and will be removed to lighten the notations. Considering the material derivative term, the variational formulation of the vesicle problem with penalty is expressed as follows:

[**Model B**]: find $\boldsymbol{u} \in C^0\left((0,T), L^2(\Lambda)^d\right) \cap L^2\left((0,T), \mathbb{V}(\boldsymbol{u}_b)\right)$, $p \in L^2\left((0,T), L^2_0(\Lambda)\right)$, and $\varphi \in C^0\left((0,T), L^2(\Lambda)^d\right) \cap L^2\left((0,T), \mathbb{X}(\varphi_b)\right)$ such that

$$\begin{aligned} &\text{Re} \int_{\Lambda} \left(\frac{\partial \boldsymbol{u}}{\partial t} + \boldsymbol{u} \cdot \nabla \boldsymbol{u} \right) \cdot \boldsymbol{v} + \int_{\Lambda} 2 \left(\mathcal{H}_\varepsilon(\varphi) + \beta \left(1 - \mathcal{H}_\varepsilon(\varphi)\right)\right) |2\mathbf{Du}|^{\varsigma-1} \mathbf{Du} : \mathbf{Dv} - \int_{\Lambda} p \, div \boldsymbol{v} \\ &+ \frac{1}{\epsilon} \int_{\Lambda} |\boldsymbol{\nabla} \varphi| \delta_\varepsilon(\varphi) div_s(\boldsymbol{u}) div_s(\boldsymbol{v}) - \frac{1}{2\text{Bn}} \int_{\Lambda} |\boldsymbol{\nabla} \varphi| \delta_\varepsilon(\varphi) \left(2\Psi + H^3\right) \mathbf{n} \cdot \boldsymbol{v} = 0, \qquad \forall \boldsymbol{v} \in \mathbb{V}(0), \end{aligned} \tag{3.4a}$$

$$\int_{\Lambda} q \, div \boldsymbol{u} = 0, \qquad \forall q \in L^2_0(\Lambda), \tag{3.4b}$$

$$\int_{\Gamma} \Psi \zeta + \int_{\Gamma} \underset{s}{\boldsymbol{\nabla}} H \cdot \underset{s}{\boldsymbol{\nabla}} \zeta = 0, \qquad \forall \zeta \in H^1(\Gamma), \tag{3.4c}$$

$$\int_{\Lambda} \frac{\partial \varphi}{\partial t} \psi + \int_{\Lambda} (\boldsymbol{u} \cdot \boldsymbol{\nabla} \varphi) \psi + \int_{\Lambda} S(\tau_K; \varphi, \psi) = 0, \qquad \forall \psi \in H^1(\Lambda). \tag{3.4d}$$

4 | FINITE ELEMENT METHOD

We consider the continuous Galerkin framework for the spatial discretization, where $\mathbb{P}_k$ denotes the piecewise continuous Lagrange polynomials of order k. We restrict our presentation on the spatial discretization of model B which presents our preferred approach for the aforementioned reasons. However, model A will serve for validation in the purely Newtonian case; we follow the numerical scheme presented in Laadhari et al. [30], with a discrete finite element space for the membrane tension based on Lagrange polynomials of the same degrees as those used for the pressure. From an implementation viewpoint, the approximation space for the Lagrange multiplier λ is defined exclusively in a small surrounding around the zero level set [40].

The inf-sup stable Taylor–Hood finite element $(\mathbb{P}_{k+1})^2 - \mathbb{P}_k$ is considered for the velocity–pressure approximation in the generalized Stokes problem [67]. For $k = 1, 2, 3, \ldots$, possibly higher order finite elements are considered using Lagrange polynomials of degrees $k+1$, k, and $k+1$ for the velocity $\boldsymbol{u}$, pressure p, and level set φ, respectively.

We introduce a shape-regular partition $\{\mathscr{T}_h\}_{h>0}$ of Λ made up of geometrically conformal triangles, this is $\overline{\Lambda}_h = \underset{K\in\mathscr{T}_h}{\cup} K$, where $h = \max_{K\in\mathscr{T}_h}\mathrm{diam}(K) > 0$ refers to the largest mesh element diameter and Λ_h is the geometric interpolation of Λ [70]. We consider the following finite-dimensional h-dependent spaces of continuous piecewise polynomial functions:

$$\begin{aligned}
\mathbb{V}_h(\boldsymbol{u}_b) &= \left\{ \boldsymbol{u} \in C^0\left(\overline{\Lambda}\right)^2, \boldsymbol{u}_{|K} \in (\mathbb{P}_{k+1}(K))^2, \forall K \in \mathscr{T}_h \right\} \cap \mathbb{V}(\boldsymbol{u}_b), \\
\mathbb{Q}_h &= \left\{ q \in \mathbb{Q} \cap C^0\left(\overline{\Lambda}\right), q_{|K} \in \mathbb{P}_k(K), \forall K \in \mathscr{T}_h \right\}, \\
\mathbb{X}_h &= \left\{ \varphi \in C^0\left(\overline{\Lambda}\right), \varphi_{|K} \in \mathbb{P}_{k+1}(K), \forall K \in \mathscr{T}_h \right\}.
\end{aligned}$$

In what follows, the subscripts h stands for the space discretized field, while $div_{s,h}(\cdot)$ refers to the discretized surface operator $\boldsymbol{\pi}_{\Gamma,h} : \boldsymbol{\nabla}(\cdot) \equiv (\mathbf{I} - \mathbf{n}_h \otimes \mathbf{n}_h) : \boldsymbol{\nabla}(\cdot)$, and $\mathbf{D}\mathbf{u}_h$ denotes $\left(\boldsymbol{\nabla}\boldsymbol{u}_h + \boldsymbol{\nabla}\boldsymbol{u}_h^T\right)/2$. The discrete variational formulation associated to (3.4a) and (3.4b) writes

Find $\mathbf{u}_h \in \mathbb{V}_h(\mathbf{u}_b)$ and $p_h \in \mathbb{Q}_h$ such that for all $\mathbf{v}_h \in \mathbb{V}_h(\boldsymbol{0})$ and $q_h \in \mathbb{Q}_h$

$$\begin{aligned}
&\mathrm{Re}\int_{\Lambda_h}\left(\frac{\partial \boldsymbol{u}_h}{\partial t} + \boldsymbol{u}_h\cdot\boldsymbol{\nabla}\boldsymbol{u}_h\right)\cdot\boldsymbol{v}_h + \int_{\Lambda_h} 2\left(\mathcal{H}_\varepsilon(\varphi_h) + \beta\left(1 - \mathcal{H}_\varepsilon(\varphi_h)\right)\right)|2\mathbf{D}\mathbf{u}_h|^{\varsigma-1}\mathbf{D}\mathbf{u}_h : \mathbf{D}\mathbf{v}_h - \int_{\Lambda_h} p_h\, div\,\boldsymbol{v}_h \\
&+ \frac{1}{\epsilon}\int_{\Lambda_h} |\boldsymbol{\nabla}\varphi_h|\delta_\varepsilon(\varphi_h)\, div_{s,h}(\boldsymbol{u}_h)\, div_{s,h}(\boldsymbol{v}_h) - \frac{1}{2\mathrm{Bn}}\int_{\Lambda_h} |\boldsymbol{\nabla}\varphi_h|\delta_\varepsilon(\varphi_h)\left(2\Psi_h + H_h^3\right)\mathbf{n}_h\cdot\boldsymbol{v}_h = 0,
\end{aligned} \tag{4.1a}$$

$$\int_{\Lambda_h} q_h\, div\,\boldsymbol{u}_h = 0. \tag{4.1b}$$

For a given time discretization scheme, the preceding finite-dimensional linear system has, from an algebraic point of view, the following generalized Stokes structure:

$$\begin{pmatrix} A & B^T \\ B & 0 \end{pmatrix}\begin{pmatrix} U \\ P \end{pmatrix} = \begin{pmatrix} F \\ 0 \end{pmatrix},$$

with U and P the vectors of degrees of freedom of $\boldsymbol{u}$ and p, respectively. For this system, standard efficient solvers exists in usual finite element libraries. It can be solved monolithically, for instance, using a Newton algorithm. We have used the preconditioned `Conjugate Gradient` and `GMRES` algorithms.

For the level set advection, a well-known spurious oscillatory instabilities occur when using the standard Galerkin discretization. To circumvent this issue, we proceed with stabilization using the streamline upwind Petrov–Galerkin (SUPG) [71]. Remark that other stabilizations can be used such as the Galerkin least squares, the sub-grid scale, and the continuous interior penalty methods [72, 73]. Accordingly, a stabilization term $S(\tau_K; \varphi, \psi)$ in (3.4d) consists in adding diffusion in the streamline direction. We choose the streamline diffusion coefficient proportional to the local mesh size h_K and depending on the advection strength at the mesh element K:

$$\tau_K = \frac{C h_K}{\max\left\{|\boldsymbol{u}|_{0,\infty,K}, \mathrm{tol}/h_K\right\}}, \ K \in \mathscr{T}_h,$$

with C a scaling factor and tol/h_K a coefficient to avoid division by zero [74]. In addition, we regularly solve for a few iterations the so-called Hamilton–Jacobi-type redistancing equation in order to straighten the level set solution as signed distance. The discretized level set advection writes

Find $\varphi_h \in \mathbb{X}_h(\varphi_b)$ such that

$$\int_{\Lambda_h} \frac{\partial \varphi_h}{\partial t} \psi_h + \int_{\Lambda_h} (\boldsymbol{u}_h \cdot \boldsymbol{\nabla}\, \varphi_h)\, \psi_h + \int_{\Lambda_h} S\,(\tau_K; \varphi_h, \psi_h) = 0, \qquad \forall \psi_h \in \mathbb{X}_h(0).$$

Let $\mathcal{I}_h^k$ stand for the L^2 projection on the discrete finite element space generated by the Lagrange polynomials of degrees k. For the discretized curvature, we proceed with a smoothed L^2 projection $\tilde{\mathcal{I}}_h^k$ using an artificial diffusion term $-\varkappa \Delta H$, see Laadhari et al. [30] and Metivet et al. [60]. We set the smoothing parameter $\varkappa = 0.03h/k$. The smoothed curvature $\tilde{\mathcal{I}}_h^k H$ satisfies

$$\int_{\Lambda_h} \tilde{\mathcal{I}}_h^k H q_h + \varkappa \int_{\Lambda_h} \boldsymbol{\nabla}\, \tilde{\mathcal{I}}_h^k H : \boldsymbol{\nabla}\, q_h - \varkappa \int_{\partial\Lambda_h} \left(\boldsymbol{\nu} \cdot \boldsymbol{\nabla}\, \tilde{\mathcal{I}}_h^k H \right) q_h = - \int_{\Lambda_h} \mathcal{I}_h^k \mathbf{n}_h \cdot \boldsymbol{\nabla}\, q_h, \qquad \forall q_h \in \mathbb{Q}_h.$$

5 | TIME DISCRETIZATION

Hereafter, we discuss the time discretization of the system of first-order differential equations that arises from the spatial discretization using finite elements. For ease of exposition, this differential system is denoted by

$$\begin{aligned} \mathbf{y}'(t) &= f(t, \mathbf{y}(t)), \ t \in [0, T], \\ \mathbf{y}(0) &= \mathbf{y}_0. \end{aligned} \tag{5.1}$$

We assume that the function f is infinitely differentiable and can be represented as the sum of its Taylor series in the neighborhood of any point. Let N be a positive integer. We consider a partition of the interval $[0, T]$ with time steps $\delta t = t_{n+1} - t_n$, where t_n for $n = 1, 2, \dots, N$ represents the discrete times. The time step δt is initially taken to be constant for simplicity, whereas we will subsequently introduce an appropriate time adaptation strategy. The subscript n denotes the value of a function at the discrete time t_n, so that $\mathbf{y}_n$ represents the time-discrete approximation of $\mathbf{y}(t_n)$. For $t > 0$, we introduce the exact flow $\mathcal{Y}_t$ of the differential system (5.1)[1]:

$$\begin{aligned} \mathcal{Y}_t &: \mathbb{R} \to \mathbb{R} \\ & \quad \mathbf{y}_0 \to \mathcal{Y}_t(\mathbf{y}_0) = \mathbf{y}(t). \end{aligned}$$

Let $\Phi_{\delta t}^{[p]}$ denote the corresponding numerical flow of a general one-step method so that $\mathbf{y}_{n+1} = \Phi_{\delta t}^{[p]}\left(\mathbf{y}_n\right)$. The approximation is of order p if the local error satisfies

$$\mathcal{Y}_{\delta t}(\mathbf{y}_0) - \Phi_{\delta t}^{[p]}(\mathbf{y}_0) = \mathcal{O}\left(\delta t^{p+1}\right).$$

The composition of numerical flows $\Phi_{a_1 \delta t}^{[p]} \circ \dots \circ \Phi_{a_s \delta t}^{[p]}$ successively used with step sizes $a_1 \delta t, \dots, a_s \delta t$ is an approximation of the exact flow at least of order $p+1$ if the algebraic conditions $a_1 + \dots + a_s = 1$ and $a_1^{p+1} + \dots + a_s^{p+1} = 0$ are satisfied [75, 76]. While the order can be increased for even p, this system has no real solutions for odd p with arbitrary s. To circumvent this problem and build up high-order methods by recursive compositions, it has been proposed the use of symmetric compositions applied to second-order methods with additional conditions [48, 75] or the use of complex time steps with positive real part [76, 77]. The latter introduces natural extensions in the complex space of time by the use of complex coefficients a_is [78].

---

[1] For clarity, we have used the usual appellations of exact and discrete flow (i.e., an integrator), which should not be confused with the flow of fluids (i.e., fluid dynamics).

5.1 | Error estimation

Theorem 1. *Consider the double composition ($s = 2$) of discrete flow $\Phi_{\delta t}^{[2]}$ associated with the CN scheme. For $n \geqslant 0$, let us denote $\mathbf{y}_{n+1,0} = \mathbf{y}_n$, $\mathbf{y}_{n+1,1} = \Phi_{a_1\delta t}^{[2]}\left(\mathbf{y}_{n+1,0}\right)$ and $\mathbf{y}_{n+1,2} = \Phi_{a_2\delta t}^{[2]}\left(\mathbf{y}_{n+1,1}\right) = \Phi_{a_2\delta t}^{[2]} \circ \Phi_{a_1\delta t}^{[2]}\left(\mathbf{y}_n\right)$. The composed numerical scheme defined by the real part $\mathbf{y}_{n+1} = Re\left(\mathbf{y}_{n+1,2}\right)$ results in a numerical method of order 4. Furthermore, the imaginary part, denoted $Im\left(\mathbf{y}_{n+1,2}\right)$, represents a corresponding error estimate to within $\mathcal{O}\left(\delta t^5\right)$.*

Proof. We first study the error on two consecutive order derivatives between the numerical and exact flows. Next, we focus on the behavior of the numerical flow with respect to any pertubation of the input $\mathbf{y}_n$ by $\epsilon > 0$. Suppose an exact solution at t_n, the approximated solution $\mathbf{y}_{n+1}$ is computed using the Crank–Nicolson scheme as follows:

$$\mathbf{y}_{n+1} = \mathbf{y}(t_n) + \frac{\delta t}{2}\left(f\left(t_n, \mathbf{y}\left(t_n\right)\right) + f\left(t_n + \delta t, \mathbf{y}_{n+1}\right)\right).$$

The solution can be obtained iteratively using a fixed point algorithm. We introduce the sequence of elements as follows:

$$\mathbf{y}_{n+1} \equiv \Phi_{\delta t}^{[2]}\left(\mathbf{y}_n\right) = \lim_{k\to\infty} Y_k, \ \text{with}\, Y_{k+1} = F\left(\mathbf{y}_n, Y_k\right) \ \text{and}\, 2F\left(\mathbf{y}_n, Y\right) = 2\mathbf{y}_n + \delta t\left(f\left(t, \mathbf{y}_n\right) + f\left(t + \delta t, Y\right)\right).$$

We compute the Taylor series expansions of Y_k at $\mathbf{y}_n$ up to order 4 and use the expressions of the derivatives $\mathbf{y}^{(l)}$, with $1 \leqslant l \leqslant 4$, in terms of the partial derivatives of f.

It follows that

$$Y_k = \mathbf{y}_n + \delta t\mathbf{y}'(t_n) + \frac{\delta t^2}{2}\mathbf{y}^{(2)}(t_n) + \frac{\delta t^3}{4}\mathbf{y}^{(3)}(t_n) + \frac{\delta t^4}{24}\left[2\mathbf{y}^{(4)} + \mathbf{y}^{(3)} f_{\mathbf{y}}\right](t_n) + \mathcal{O}\left(\delta t^5\right), \qquad \forall k \geqslant 4. \tag{5.2}$$

The first three terms in (5.2) correspond to the ones in the Taylor development of the exact solution at $t_n + \delta t$ up to third order, that is, the basic Cranck–Nicolson method is of order 2. It can be checked that $Y_{k+1} - Y_k = \mathcal{O}\left(\delta t^5\right)$, $\forall k \geqslant 4$. This means that, for $k \geqslant 4$, the terms in the Taylor development of elements Y_k are the same up to order 4. Hence, the discrete flow can be expressed at order 4 as a function of the exact flow as follows:

$$\Phi_{\delta t}^{[2]}\left(\mathbf{y}_n\right) = Y_4 = \mathcal{Y}_{\delta t}\left(\mathbf{y}_n\right) + \frac{1}{12}\delta t^3\mathbf{y}^{(3)}(t_n) + \frac{1}{24}\delta t^4\left[\mathbf{y}^{(4)} + \mathbf{y}^{(3)} f_{\mathbf{y}}\right](t_n) + \mathcal{O}\left(\delta t^5\right). \tag{5.3}$$

In the sequel, $f_{\mathbf{y}}\left(t_n, \mathbf{y}\left(t_n\right)\right)$ is shortly denoted by $f_{\mathbf{y}}(t_n)$.

We focus on the two-step composition $\Phi_{a_2\delta t}^{[2]} \circ \Phi_{a_1\delta t}^{[2]}\left(\mathbf{y}_n\right)$ at t_n. According to the above algebraic conditions, a_1 and a_2 satisfy $a_1 + a_2 = 1$ and $a_1^3 + a_2^3 = 0$ [75]. That is, $a_1 = \frac{3-i\sqrt{3}}{6}$ and $a_2 = \frac{3+i\sqrt{3}}{6}$. From (5.3), it follows that

$$\mathbf{y}_{n+1,1} = \Phi_{a_1\delta t}^{[2]}\left(\mathbf{y}_n\right) = \mathcal{Y}_{a_1\delta t}\left(\mathbf{y}_n\right) + \frac{a_1^3\delta t^3}{12}\mathbf{y}^{(3)}(t_n) + \frac{a_1^4\delta t^4}{24}\left[\mathbf{y}^{(4)} + \mathbf{y}^{(3)} f_{\mathbf{y}}\right](t_n) + \mathcal{O}\left(\delta t^5\right).$$

Consider now the second flow composition and define $\bar{\varepsilon}$ as follows:

$$\Phi_{a_2\delta t}^{[2]}\left(\Phi_{a_1\delta t}^{[2]}\left(\mathbf{y}_n\right)\right) = \Phi_{a_2\delta t}^{[2]}\left(\mathcal{Y}_{a_1\delta t}\left(\mathbf{y}_n\right) + \underbrace{\frac{a_1^3\delta t^3}{12}\mathbf{y}^{(3)}(t_n) + \frac{a_1^4\delta t^4}{24}\left[\mathbf{y}^{(4)} + \mathbf{y}^{(3)} f_{\mathbf{y}}\right](t_n) + \mathcal{O}\left(\delta t^5\right)}_{\bar{\varepsilon}}\right). \tag{5.4}$$

By employing the perturbation theory, the Taylor expansion of f at y_n gives

$$\Phi_{\delta t}^{[2]}\left(\mathbf{y}_n + \bar{\varepsilon}\right) = \Phi_{\delta t}^{[2]}\left(\mathbf{y}_n\right) + \bar{\varepsilon} + \bar{\varepsilon}\delta t f_{\mathbf{y}}(t_n) + \mathcal{O}\left(\bar{\varepsilon}\delta t^2\right). \tag{5.5}$$

Starting from $\mathbf{y}(t_n + a_1\delta t)$ with a step size $a_2\delta t$, it follows that

$$\Phi^{[2]}_{a_2\delta t}\left(\varphi_{a_1\delta t}\left(\mathbf{y}_n\right) + \bar{\varepsilon}\right) = \Phi^{[2]}_{a_2\delta t}\left(\mathbf{y}(t_n + a_1\delta t)\right) + \bar{\varepsilon} + \bar{\varepsilon} a_2 \delta t f_{\mathbf{y}}(t_n + a_1\delta t) + \mathcal{O}\left(\bar{\varepsilon}\delta t^2\right). \tag{5.6}$$

By using $\mathcal{O}\left(\bar{\varepsilon}\delta t^2\right) = \mathcal{O}\left(\delta t^5\right)$, we substitute $\bar{\varepsilon}$ by its expression in (5.4) and express (5.6) as follows:

$$\Phi^{[2]}_{a_2\delta t}\left(\Phi^{[2]}_{a_1\delta t}\left(\mathbf{y}_n\right)\right) = \Phi^{[2]}_{a_2\delta t}\left(\mathcal{Y}_{a_1\delta t}\left(\mathbf{y}_n\right)\right) + \frac{a_1^3\delta t^3}{12}\mathbf{y}^{(3)}(t) + \frac{\delta t^4}{24}\left[a_1^4\mathbf{y}^{(4)} + (a_1^4 + 2a_2a_1^3)\mathbf{y}^{(3)} f_{\mathbf{y}}\right](t_n) + \mathcal{O}\left(\delta t^5\right). \tag{5.7}$$

Using (5.3) with a step $a_2\delta t$, we approximate the discrete flow $\Phi^{[2]}_{a_2\delta t}\left(\mathcal{Y}_{a_1\delta t}\left(\mathbf{y}_n\right)\right)$ with respect to the exact one $\mathcal{Y}_{\delta t}\left(\mathbf{y}_n\right)$:

$$\Phi^{[2]}_{a_2\delta t}\left(\mathcal{Y}_{a_1\delta t}\left(\mathbf{y}_n\right)\right) = \mathcal{Y}_{a_2\delta t}\left(\mathbf{y}(t_n + a_1\delta t)\right) + \frac{a_2^3\delta t^3}{12}\mathbf{y}^{(3)}(t_n + a_1\delta t) + \frac{a_2^4\delta t^4}{24}\left[\mathbf{y}^{(4)} + \mathbf{y}^{(3)} f_{\mathbf{y}}\right](t_n + a_1\delta t) + \mathcal{O}\left(\delta t^5\right). \tag{5.8}$$

For the perturbation $a_1\delta t$, we show, using the Taylor developments of third and fourth derivatives of $\mathbf{y}$ at t_n, that

$$\Phi^{[2]}_{a_2\delta t}\left(\mathcal{Y}_{a_1\delta t}\left(\mathbf{y}_n\right)\right) = \mathcal{Y}_{a_2\delta t}\left(\mathcal{Y}_{a_1\delta t}\left(\mathbf{y}_n\right)\right) + \frac{a_2^3\delta t^3}{12}\mathbf{y}^{(3)}(t_n) + \frac{\delta t^4}{24}\left[\left(a_2^4 + 2a_1a_2^3\right)\mathbf{y}^{(4)} + a_2^4\mathbf{y}^{(3)} f_{\mathbf{y}}\right](t_n) + \mathcal{O}\left(\delta t^5\right). \tag{5.9}$$

Substituting $\Phi^{[2]}_{a_2\delta t}\left(\mathcal{Y}_{a_1\delta t}\left(\mathbf{y}_n\right)\right)$ in (5.7) with its expression in (5.9), we obtain

$$\begin{aligned}\mathbf{y}_{n+1,2} \equiv \Phi^{[2]}_{a_2\delta t}\left(\Phi^{[2]}_{a_1\delta t}\left(\mathbf{y}_n\right)\right) &= \mathcal{Y}_{a_2\delta t}\left(\mathcal{Y}_{a_1\delta t}\left(\mathbf{y}_n\right)\right) + \frac{\delta t^3}{12}\left(a_1^3 + a_2^3\right)\mathbf{y}^{(3)}(t_n) \\ &+ \frac{\delta t^4}{24}\left[\left(a_1^4 + 2a_2^3a_1 + a_2^4\right)\mathbf{y}^{(4)} + \left(a_1^4 + 2a_1^3a_2 + a_2^4\right)\mathbf{y}^{(3)} f_{\mathbf{y}}\right](t_n) + \mathcal{O}\left(\delta t^5\right).\end{aligned}$$

Using the conditions $a_1 + a_2 = 1$ and $a_1^3 + a_2^3 = 0$ and the propriety $\mathcal{Y}_{\gamma_1} \circ \mathcal{Y}_{\gamma_2} = \mathcal{Y}_{\gamma_1+\gamma_2}$ for any γ_1 and γ_2, we obtain

$$\mathbf{y}_{n+1,2} = \Phi^{[2]}_{a_2\delta t}\left(\Phi^{[2]}_{a_1\delta t}\left(\mathbf{y}_n\right)\right) = \mathcal{Y}_{\delta t}\left(\mathbf{y}_n\right) + \frac{\delta t^4}{24}\left[a_2^3\mathbf{y}^{(4)} + a_1^3\mathbf{y}^{(3)} f_{\mathbf{y}}\right](t_n) + \mathcal{O}\left(\delta t^5\right). \tag{5.10}$$

As a consequence, the composed flow in Equation (5.10) is an approximation of the exact solution $\mathbf{y}(t_{n+1}) \equiv \mathcal{Y}_{\delta t}\left(\mathbf{y}_n\right)$ at $t_n + \delta t$ at least of order 3, thus giving $\mathbf{y}_{n+1} = \mathrm{Re}\left(\mathbf{y}_{n+1,2}\right)$. In addition, we use $9a_2^3 = i\sqrt{3} = -9a_1^3$ to prove the following approximation error estimate:

$$e_{\delta t}(t_n + \delta t) = \mathcal{Y}_{\delta t}\left(\mathbf{y}_n\right) - \mathrm{Re}\left(\mathbf{y}_{n+1,2}\right) = \frac{\delta t^4}{24}\left(\mathrm{Re}\left(a_2^3\right)\mathbf{y}^{(4)} + \mathrm{Re}\left(a_1^3\right)\mathbf{y}^{(3)} f_{\mathbf{y}}\right)(t_n) + \mathcal{O}\left(\delta t^5\right) = \mathcal{O}\left(\delta t^5\right), \tag{5.11}$$

which implies that the local truncation error is within $\mathcal{O}\left(\delta t^5\right)$. Then, the real part of the composition (5.10) behaves as a fourth-order integrator, higher than the order of the original CN method. Here, we suppose that the derivatives of f, up to third order, are bounded. Moreover, the imaginary part

$$\begin{aligned}\mathrm{Im}\left(\mathbf{y}_{n+1,2}\right) =& \frac{\delta t^4}{24}\left(\mathrm{Im}\left(a_2^3\right)\mathbf{y}^{(4)} + \mathrm{Im}\left(a_1^3\right)\mathbf{y}^{(3)} f_{\mathbf{y}}\right)(t_n) + \mathrm{Im}\left(\mathcal{O}\left(\delta t^5\right)\right) \\ =& \frac{\sqrt{3}\delta t^4}{216}\left(\mathbf{y}^{(4)} - \mathbf{y}^{(3)} f_{\mathbf{y}}\right)(t_n) + \mathrm{Im}\left(\mathcal{O}\left(\delta t^5\right)\right),\end{aligned} \tag{5.12}$$

represents an alternative error indicator of the approximated solution $\mathbf{y}_{n+1} = \mathrm{Re}\left(\mathbf{y}_{n+1,2}\right)$ at least of order 3. This gives

$$\left|e_{\delta t}(t_n + \delta t) - \mathrm{Im}\left(\mathbf{y}_{n+1,2}\right)\right| = \frac{\sqrt{3}\delta t^4}{216}\left|\mathbf{y}^{(4)} - \mathbf{y}^{(3)} f_{\mathbf{y}}\right|(t_n) + \mathcal{O}\left(\delta t^5\right).$$

$\square$

5.2 | Adaptive time stepping

While the use of a uniformly large time step can produce unphysical solutions, the use of larger time steps when some slow dynamics hold (e.g., around the horizontal position during the so-called tumbling regime) allows to reduce the computational cost. We set upper δt_{max} and lower δt_{min} bounds of the time-step size to avoid abrupt variations. It therefore follows that the aforementioned imaginary part can represent a precise criterion for controlling the temporal integration error and will therefore be used as error estimator for the adaptive time-step scheme. The goal is a computation with adaptively determined time-step sizes, so that the time integration error does not exceed a prescribed threshold value. Given the above error indicator $\varsigma_{n+1} = \mathrm{Im}\left(\mathbf{y}_{n+1,2}\right)$ at each time step, the adaptive time step δt_{n+1} is set as follows:

$$\delta t_{n+1} = \min\left\{ \max\left\{ \delta t_{min}, \delta t_n \left(\frac{tol}{C\|\varsigma_{n+1}\|_{L^2(\Lambda)}} \right)^{1/p} \right\}, \delta t_{max} \right\}.$$

The predefined parameter C helps to adjust the level of adaptability while *tol* is the desired error tolerance so that small time steps are generated for large errors and vice versa. The parameter p is the obtained order by composition method. A comparison in terms of computational accuracy will also be made versus a conventional change rate criterion $\|\partial_{\delta t}\varphi_n\| = \|\varphi_{n+1} - \varphi_n\|/\delta t_n$ between consecutive numerical solutions [79, 80]. Here, the adaptive time step δt_{n+1} is

$$\delta t_{n+1} = \max\left\{ \delta t_{min}, \frac{\delta t_{max}}{\sqrt{1 + C\|\partial_{\delta t}\varphi_n\|^2}} \right\}.$$

Remark 1. We follow Laadhari et al. [30, 40] and perform an a posteriori mass correction in the advection equation to enforce the global mass conservation (area and perimeter in 2D) at the end of every time step. Similar techniques are used in Eulerian approaches; see, for example, previous studies [36, 81, 82]. A modified advection equation includes a forcing term $\vartheta(t_n)$ in $\frac{\partial\varphi}{\partial t} + \boldsymbol{u} \cdot \nabla\varphi\Big|_{t=t_n} = \vartheta(t_n)$ under the global constraints $|\Omega(t_n)| = |\Omega(t_0)|$ and $|\Gamma(t_n)| = |\Gamma(t_0)|$, see Laadhari et al. [40] for a detailed description.

Remark 2. Solving the two-way coupled fluid/membrane problem sequentially affects the convergence and stability of the solution. To circumvent the instabilities of loosely coupled strategies, we enforce the coupling conditions at every time step using an iterative fixed point process between the level set and the fluid solvers. This strongly coupled iterative approach generally requires only a few iterations at each time step.

6 | NUMERICAL EXPERIMENTS

The computations were conducted using FEniCSx [83] and the Rheolef [84] C++ libraries for scientific computing. Rheolef utilizes Message Passing Interface (MPI)[2] for parallelism on distributed-memory architectures, while MUMPS is used for factorization and as direct solver. Additionally, it relies on the Boost,[3] Basic Linear Algebra Subprograms (BLAS),[4] and SCOTCH[5] libraries to provide various functionalities. The visualization and figures were generated using Paraview [85] and Gnuplot [86].

6.1 | Example 1: Ordinary differential equation test case—Convergence study

We test the accuracy of the composition approach in solving the following stiff Cauchy problem:

$$\frac{dy}{dt} + \tan(t-2)y = \alpha\cos(t-2)\,\frac{(t-2)(t-5) + (t-2)(t-8) + (t-5)(t-8)}{1 + \alpha(t-2)^2(t-5)^2(t-8)^2},$$
$$\text{with initial condition} \quad y(0) = y_0.$$

---

[2] MPI—https://www.mpich.org.
[3] Boost—https://www.boost.org.
[4] BLAS—https://www.netlib.org/blas.
[5] SCOTCH—https://www.labri.fr/perso/pelegrin/scotch.

The exact solution

$$y(t) = 3\cos(t-2)\arctan\left(\alpha(t-2)(t-5)(t-8)\right)$$

features stiff variations at times $t = 2$, $t = 5$, and $t = 8$. We first choose the parameter $\alpha = 1$ and carry out a study of convergence versus the step size δt for different numerical schemes. The errors between the numerical and exact solutions are reported in Figure 2. They corroborate the theoretical orders of convergence, showing optimal convergences for the backward Euler $\Phi^{[1]}$ and Cranck–Nicolson $\Phi^{[2]}$ schemes, while a higher fourth-order convergence is achieved by twice composition of the CN integrator.

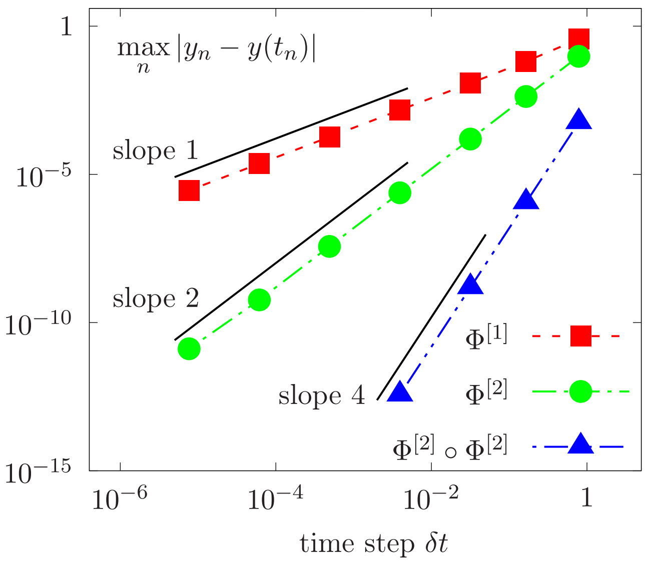

FIGURE 2 Example 1: Time convergence analysis showing the error in the L^∞ norm as a function of the time step for the backward Euler $\Phi^{[1]}$ and Crank–Nicolson $\Phi^{[2]}$ schemes. Uniform time steps are used. [Colour figure can be viewed at wileyonlinelibrary.com]

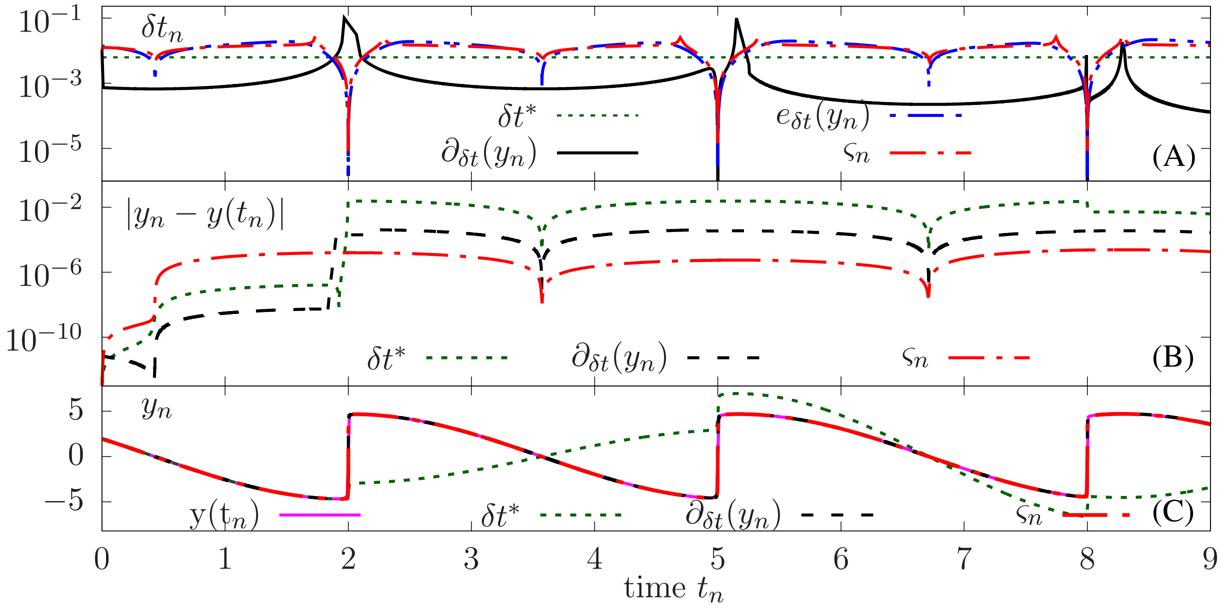

FIGURE 3 Example 1: Comparative study of accuracy using various error estimates for the adaptive time-stepping strategies, as well as uniform time-step size $\delta t^\star$ allowing the same number of iterations obtained with the imaginary criterion. [Colour figure can be viewed at wileyonlinelibrary.com]

We compare the time-stepping strategies for different criteria with higher stiffness parameter $\alpha = 100$. Consider the composition of the Cranck–Nicolson and set the tolerance of 10^{-10}. We solve the initial value problem using a uniform time step δt^* and variable time steps adapted according to different criteria (i) the exact error with respect to the exact solution, (ii) the imaginary error estimate ς_n, and (iii) the rate of change $|\partial_{\delta t}(y_n)|$. Figure 2A depicts perfect agreement in adapting δt_n using the error estimate based on the imaginary part and the exact evaluation of error. Indeed, the imaginary criterion helps to capture the stiff solution with an appropriate level of time adaptivity compared to the strategy using the rate of change $|\partial_{\delta t}(y_n)|$ as a criterion or the use of a constant time step. See the corresponding errors with respect to the exact solution and the numerical solutions in Figure 3B,C. Furthermore, the strategy based on the imaginary criteria ς_n requires 3084 total subintervals, yielding lower computational cost compared to the use of the criterion $|\partial_{\delta t}(y_n)|$ requiring 25,726 adapted time steps.

In order to assess the accuracy of the time discretization with respect to a classic method, we conduct a comparative study between our composed Crank–Nicolson scheme and the fourth-order Runge–Kutta (RK4) method. The RK4 method is a one-step method, where the solution at each time step is approximated by incorporating a weighted average of four increments corresponding to the stages of the RK4 scheme, starting from the current solution y_n. Consider the stiff differential equation with a relatively large stiffness parameter $\alpha = 50$. The numerical integration is performed over the time interval $[0, 9]$. The composed Crank–Nicolson scheme is applied with an adaptive time-stepping strategy based on the theoretical estimation of the approximation error obtained with the imaginary part criterion ς_n at each discrete time t_n.

Due to the absence of an exact error estimation for the discrete flow $\Phi^{[4]}_{\mathrm{RK4}}$ associated with the RK4 method, we adopt a numerical resolution involving either a fixed time step $\delta t^{\star}$ or an adaptive time-stepping strategy based on the rate of change criterion $\partial_{\delta t}(y_n)$. Figure 4C plots the numerical solutions obtained using various methods. It demonstrates the difficulties in accurately capturing the stiffness of the solution when using the Runge–Kutta method with a fixed time-step size. However, employing an adaptive step size based on the rate of change criterion leads to visually improved results.

To quantitatively assess the accuracy, we analyze the local error in time in Figure 4B. Remark that the RK4 method with uniform time steps exhibits a loss of accuracy in the stiffness zone, with an error on the order of 1. On the other hand, the adapted Crank–Nicolson method maintains the approximation error below 10^{-6}. While the use of the rate of change criterion improves the error for the RK4 method, it still remains significantly less accurate compared to the Crank–Nicolson method.

Figure 4A demonstrates the efficiency of time-step adaptation using the criterion ς_n against an exact evaluation of the error $e_{\delta t}(y_n)$ based on the exact analytical solution. The time step is appropriately reduced in the high stiffness region, resulting in accurate numerical approximations. Thus, the fourth-order composed Crank–Nicolson scheme with adaptive time steps, guided by the theoretical error estimate, outperforms the RK4 method (which has no error estimate) in terms of accuracy.

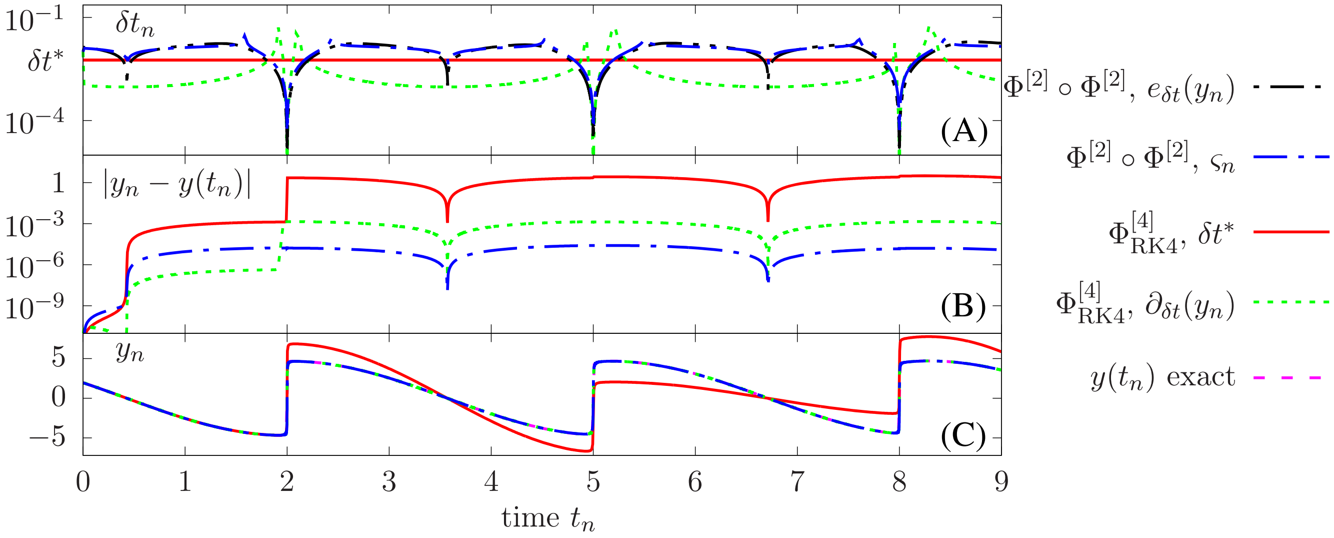

FIGURE 4 Example 1: Comparative study of accuracy between the composed Cranck–Nicolson and Runge–Kutta 4, referred to as $\Phi^{[4]}_{\mathrm{RK4}}$, using both uniform time step $\delta t^{\star}$ and adaptive time steps based on the rate of change criterion. [Colour figure can be viewed at wileyonlinelibrary.com]

In the following, we conduct a comparative study of the computational cost for successively refined temporal discretizations with fixed time steps. The results are depicted in Figure 5, showcasing the CPU time as a function of the global error computed relative to the exact solution. As expected, the CPU time increases as the desired level of precision rises for both the composed Crank–Nicolson and RK4 schemes. However, note that at higher levels of computational accuracy, the composed Crank–Nicolson scheme outperforms the RK4 scheme by enabling more significant improvements in accuracy through the refinement of the discretization. Indeed, the RK4 scheme is known to perform well when the problem is non-stiff. However, in the context of stiff problems, the RK4 scheme demonstrates a slower improvement of accuracy, posing difficulties in attaining high levels of precision. This observation aligns with some remarks reported in the literature, see, for example, Deeb et al. [52].

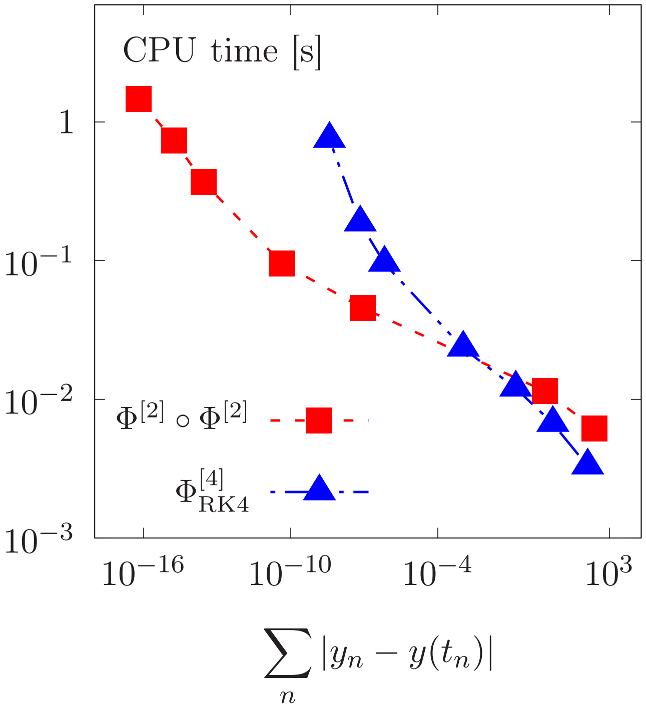

FIGURE 5 Example 1: Variation in computational cost as a function of global accuracy for the composed Crank–Nicolson and Runge–Kutta 4 schemes. [Colour figure can be viewed at wileyonlinelibrary.com]

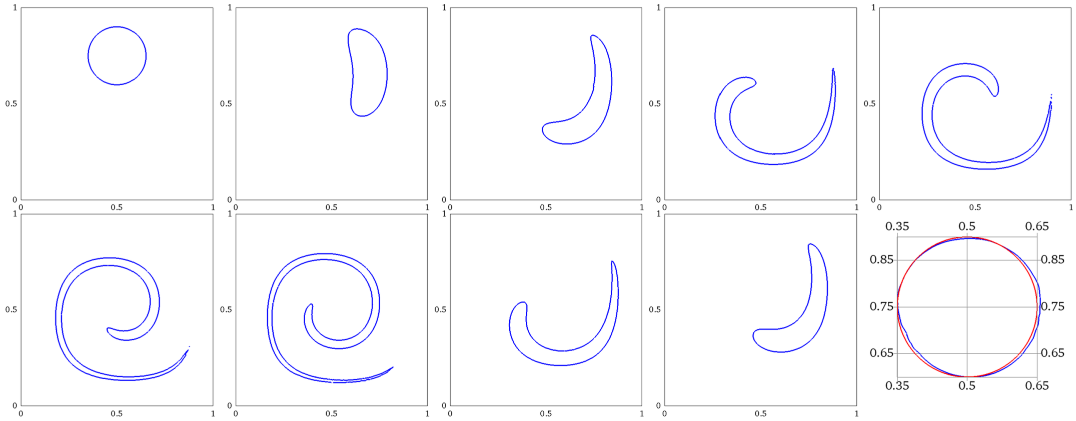

FIGURE 6 Example 2: Snapshots showing the stretching of an initially circular vortex at successive times $t = 0, 0.264, 0.85, 1.05, 1.362, 2.034, 3, 5.154, 5.46, 6$. Shape of the interface at final time $t = 6$ (blue color) compared to the exact solution (red color). [Colour figure can be viewed at wileyonlinelibrary.com]

6.2 | Example 2: Level set problem—Space and time convergence

We present a numerical test to assess the capabilities and effectiveness of the level set solver and composition technique in increasing accuracy and solving the level set problem with high-order finite elements. We consider the reversible "vortex-in-a-box" test characterized by large interface deformations and usually used to evaluate Eulerian methods for capturing thin filaments in stretched interface at the mesh scale.

Consider a unit computational domain, a circular interface of radius $R = 0.15$ initially placed at $(0.5, 0.75)$ is largely deformed periodically using an advection field defined through a stream function introduced in Bell et al. [87]:

$$\Psi = \frac{1}{\pi}\sin^2(\pi x)\sin^2(\pi y), \text{ with } \boldsymbol{x} = (x, y)^T \in \Lambda.$$

The time-reversed vortex problem introduced in LeVeque [88, Example 9.5] consists in setting the solenoidal velocity field:

$$\boldsymbol{u}(t, \boldsymbol{x}) = \begin{pmatrix} -\frac{\partial \Psi}{\partial y}\cos\left(\pi \frac{t}{T}\right) \\ \frac{\partial \Psi}{\partial x}\cos\left(\pi \frac{t}{T}\right) \end{pmatrix} = \begin{pmatrix} -2\sin(\pi x)^2 \sin(\pi y)\cos(\pi y)\cos\left(\pi \frac{t}{T}\right) \\ 2\sin(\pi y)^2 \sin(\pi x)\cos(\pi x)\cos\left(\pi \frac{t}{T}\right) \end{pmatrix}, \text{ with } t \in [0, T], \boldsymbol{x} = (x, y)^T \in \Lambda.$$

The multiplication by the cosine term makes it possible to introduce the periodicity of the deformations and to evaluate the error on the deformations of the vortex. The fluid is centrifuged and stretched out the circular interface which winds towards the center of the vortex until reaching a maximum deformation at time $T/2$. The vortex ends up resuming its initial circular shape after one period, chosen $T = 6$, while a major difficulty consists in representing the interface precisely in the zones of fine filaments close to the size of the local mesh. Figure 6 shows consecutive snapshots of the interface deformations using constant time step $\delta t = 6 \times 10^{-3}$ and unstructured mesh $h = 1/80$ with a comparison of the interface obtained after one period with the exact one.

We evaluate the spatial accuracy by computing the error

$$e_h(\varphi) = \|\mathcal{H}_\varepsilon(\varphi_h) - \mathcal{H}_\varepsilon(\pi_h \varphi)\|_{\kappa,\Lambda}, \ \kappa \in \{1, 2, \infty\},$$

for different Lagrange polynomials $\mathbb{P}_k$ with $k \geqslant 1$, on successively refined meshes with respect to the exact solution at the final time $t = T$. The time step is set small enough not to overcome spatial errors. The error history is plotted in Figure 7 show that the errors obey a convergence of $\mathcal{O}\left(h^k\right)$, $\mathcal{O}\left(h^{k-1/2}\right)$, and $\mathcal{O}\left(h^{k-1}\right)$, respectively, in norms L^1, L^2, and L^∞.

We proceed with a comparative analysis of the computational cost between the composed Crank–Nicolson scheme and the classic RK4 scheme, both of fourth-order accuracy. The simulations are performed using fixed time steps, and the level set problem is solved on successively refined meshes. The corresponding CPU times are presented in Tables 1 and 2, employing $\mathbb{P}_1$ and $\mathbb{P}_2$ piecewise finite element approximations, respectively. The results demonstrate that the composed

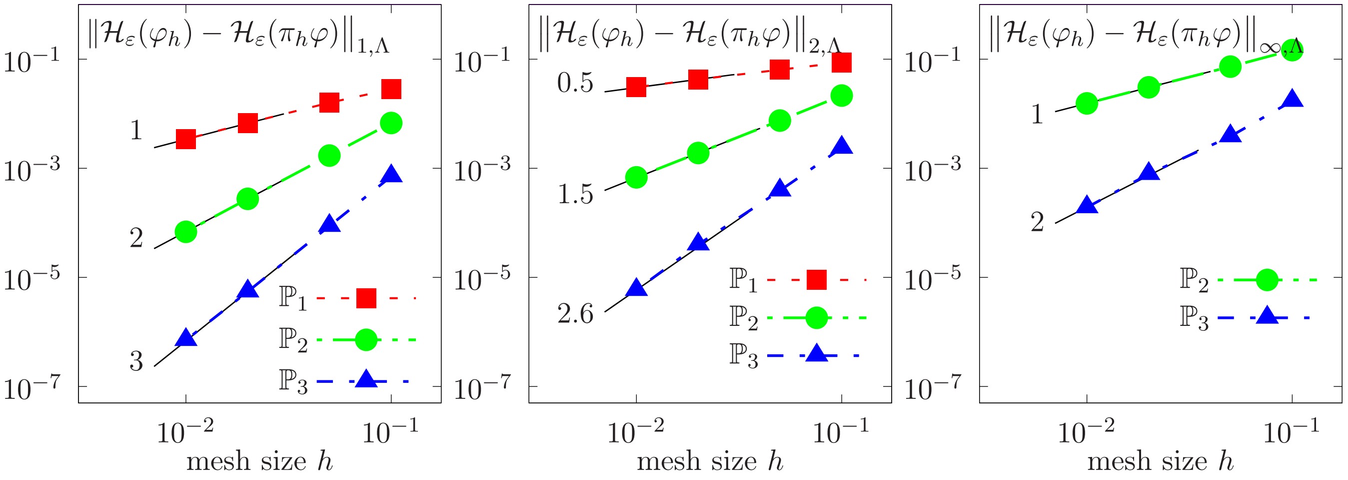

FIGURE 7 Example 2: Study of convergence in $L^\kappa(\Lambda)$ norms, with $\kappa = 1, 2, \infty$, with respect to the spatial resolution versus different Lagrange polynomials $\mathbb{P}_k$ with $k = 1, 2, 3$. [Colour figure can be viewed at wileyonlinelibrary.com]

	CPU time (s)	
h	$\Phi^{[2]} \circ \Phi^{[2]}$	$\Phi^{[4]}_{\mathrm{RK4}}$
10^{-1}	14.946	23.238
5.00×10^{-2}	25.735	39.688
2.00×10^{-2}	107.333	156.092
1.25×10^{-2}	265.708	393.465
10^{-2}	429.387	644.161
7.14×10^{-3}	914.649	1405.193
5.00×10^{-3}	2090.565	4313.484

Note: Uniform time steps are considered.

TABLE 1 Example 2: Comparative study of the computational cost between the composed Cranck–Nicolson and Runge–Kutta 4, referred to as $\Phi^{[4]}_{\mathrm{RK4}}$, schemes with $\mathbb{P}_1$ finite element approximations.

	CPU time (s)	
h	$\Phi^{[2]} \circ \Phi^{[2]}$	$\Phi^{[4]}_{\mathrm{RK4}}$
10^{-1}	25.553	38.999
5.00×10^{-2}	86.507	166.372
2.00×10^{-2}	342.734	826.524
1.25×10^{-2}	1180.585	2547.375
10^{-2}	1804.125	3274.211
5.00×10^{-3}	11,373.279	32,416.874

TABLE 2 Example 2: Comparative study of the computational cost using the composed Cranck–Nicolson and RK4 schemes with $\mathbb{P}_2$ finite element approximations. Uniform time steps are considered.

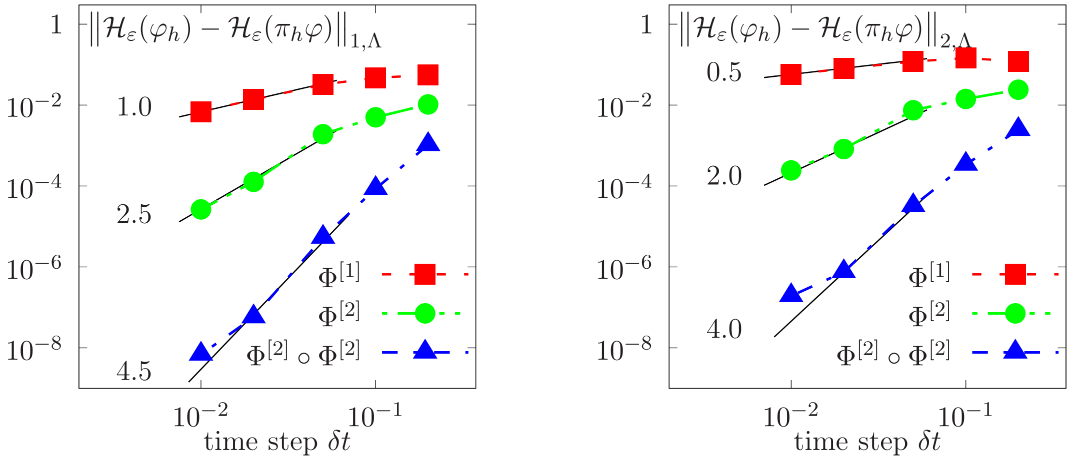

FIGURE 8 Example 2: Comparative study of the convergence rates in time for various numerical schemes. The errors are computed in the $L^\kappa(\Lambda)$ norms with $\kappa = 1, 2$. [Colour figure can be viewed at wileyonlinelibrary.com]

Crank–Nicolson scheme provides substantial computational savings compared to the RK4 scheme. Indeed, as the mesh sizes become finer, the computational cost of the RK4 scheme nearly doubles. This increase in cost is primarily due to the need for multiple resolutions of linear systems.

We also study the temporal accuracy by calculating the errors for uniform time steps and sufficiently small mesh after one deformation period. Figure 8 shows convergence rates improved by flow compositions. Moreover, the temporal accuracy of numerical approximations is studied by calculating the error in $\mathcal{H}_\varepsilon(\varphi_h)$ for successively refined time steps. The errors are computed after one deformation period in both norms L^1 and L^2 using the backward Euler, the Cranck–Nicolson, and the two time composition of the Cranck–Nicolson scheme. As expected, the results in Figure 8 depicts faster convergence when using the CN compared to the BE scheme. Moreover, the convergence rates are enhanced by composition of numerical flow.

6.3 | Example 3: Dynamics of single vesicle in simple shear flow

Consider a vesicle of reduced area $\Xi_{2D} = 0.73$ immersed in a fluid subjected to shear. We run simulations using an unstructured mesh with a mesh size $h = 0.01$. Although inertial effects play an important role in determining vesicle motion as investigated in previous studies [4, 65, 91], this is beyond the scope of this work. The vesicle is released with

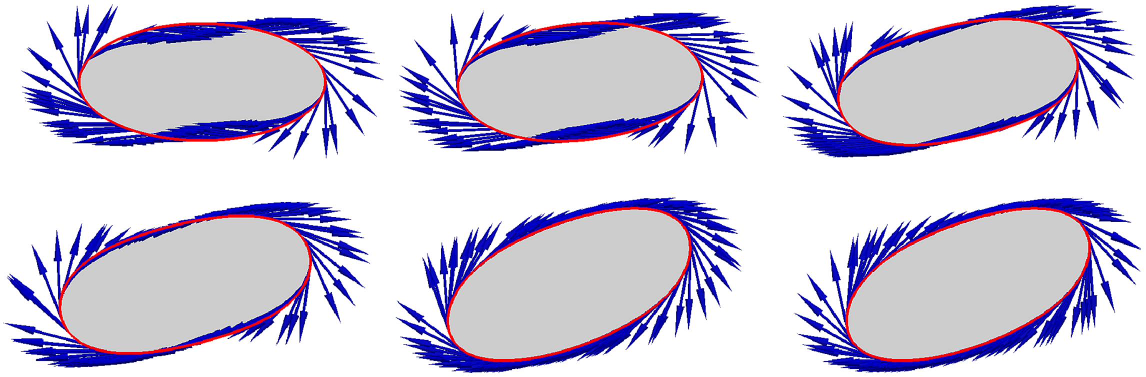

FIGURE 9 Example 3: Dynamics of a vesicle with reduced area $\Xi_{2D} = 0.73$ following a tank-treading (TT) regime in simple shear flow conditions at times $t \in \{0, 0.1, 0.3, 3, 5, 10\}$. Snapshots also display the velocity field on the membrane, which becomes tangential when steady state is reached. [Colour figure can be viewed at wileyonlinelibrary.com]

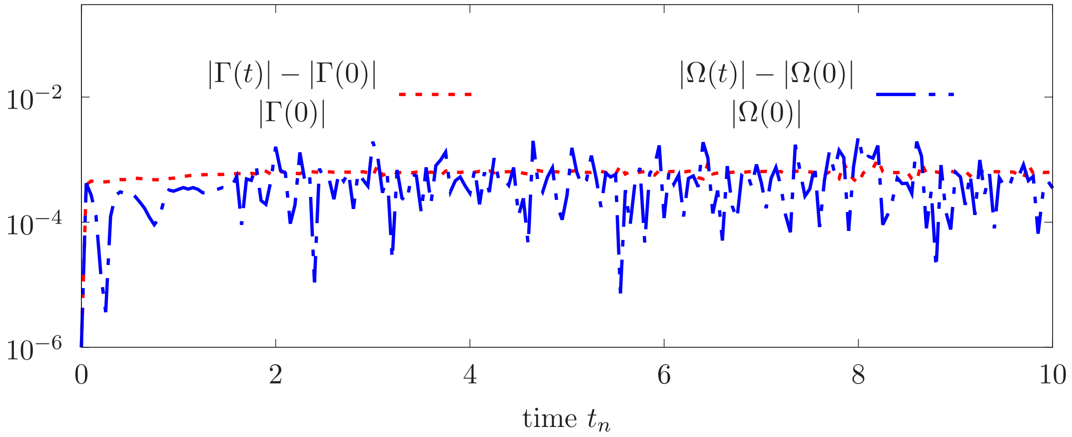

FIGURE 10 Example 3: Evolution over time of the relative area $|\Omega|$ and the relative perimeter $|\Gamma|$ of the vesicle in a TT movement. Good mass conservation properties are obtained. [Colour figure can be viewed at wileyonlinelibrary.com]

$Re = 10^{-2}$, a typical value for inertia in small capillaries. According to an experimental analysis [92], RBCs in the two-dimensional case under simple shear flow can undergo two particular behaviors: tank-treading (denoted by TT) and tumbling (denoted by TB) motions. An important parameter in this dynamics is the viscosity ratio β. The motion regime is however known to be insensitive to other parameters such as the bending Bn and the density ratio, see e.g. [4].

We first choose $\beta = 1$. Snapshots showing vesicle dynamics are provided in Figure 9. Starting from a horizontal position, the membrane started moving until a certain equilibrium configuration is achieved, for which it fixes its main axis at a given orientation with respect to the external flow direction and continues to rotate; this is the TT regime. When the steady-state angle is reached, the fluid velocity field becomes tangent to the membrane, which is superimposed on the streamlines. It has been shown that the angle of equilibrium depends only on the reduced area; see Laadhari et al. [40] and Kraus et al. [89]. Given the importance of incompressibility and inextensibility for biomembranes, we plot in Figure 10 the evolution of the error in global surface and perimeter of the vesicle as a function of time. Results depicts a good mass conservation property, as the the mass loss is kept below 0.1%.

We proceed with a quantitative validation with respect to some numerical and experimental results known in the literature. Simulations are performed in both Newtonian and non-Newtonian suspending fluids cases for several reduced areas $\Xi_{2D} \in [0.6, 0.9]$. We report in Figure 11 the steady-state inclination angle, denoted by θ^*. For the Newtonian case, the numerical results using model A with the mixed formulation are globally in agreement with the available results, in particular with those obtained by Salac et al. who also used the level set formalism with a mixed formulation in a finite difference framework. The equilibrium angle approaches $\pi/4$ as the shape becomes more circular, while its value decreases as the vesicle becomes more deflated. With model B, the curve has a qualitatively similar profile but with higher equilibrium angles. This is due to the regularization of the inextensibility constraint which is not imposed any more in an exact way.

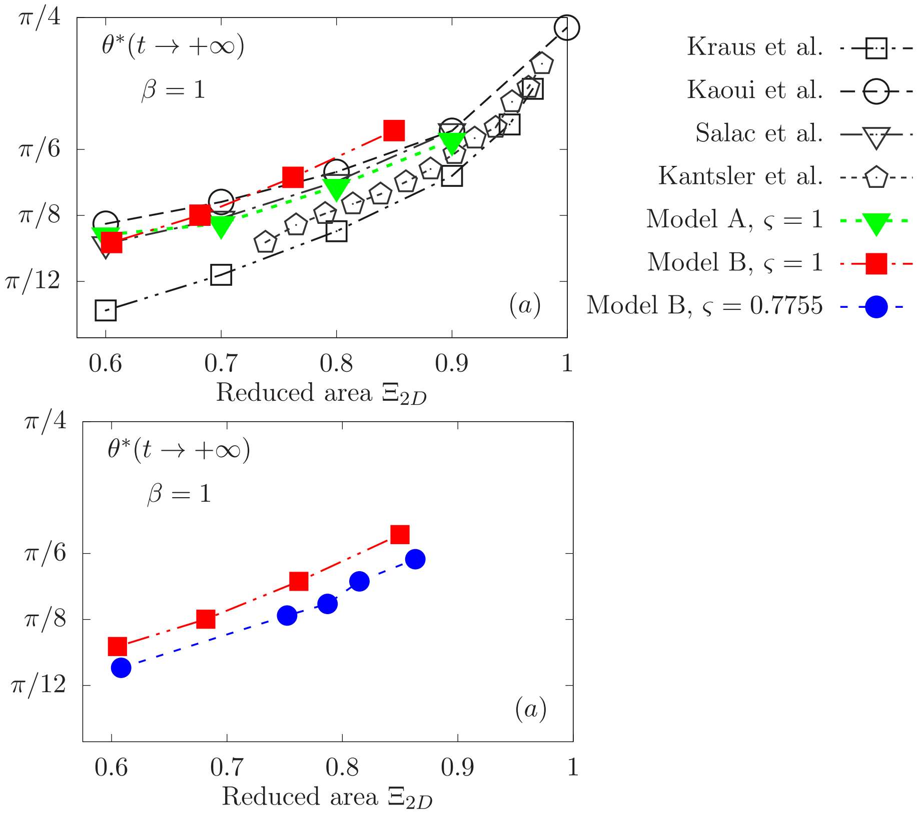

FIGURE 11 Example 3: Vesicle in the steady tank-treading regime. Change in the equilibrium inclination angle θ^* versus the reduced area Ξ_{2D} for $\beta = 1$, Re $= 10^{-3}$, and Bn $= 10^2$. Comparisons with the published results from Salac and Miksis [66] (Re $= 10^{-3}$ and Bn $= 10^2$), Kraus et al. [89] (Bn $= 10$), Kaoui et al. [28] (Bn $= 1$, $\gamma = 0.4$), and the experimental results in Kantsler and Steinberg [90]. [Colour figure can be viewed at wileyonlinelibrary.com]

Using the non-Newtonian fluid model with the penalty model, the vesicle also follows the TT motion as the angle of inclination at equilibrium decreases when stepping down Ξ_{2D}. However, the curve is shifted downward. That is, the steady-state TT inclination becomes closed to the horizontal position for the same reduced area relative to the Newtonian frame.

We now proceed to an increase in the viscosity ratio between the encapsulated fluid and the surrounding fluid, and we choose $\beta = 10$. In accordance with a known theory, a change in the dynamics regime holds and the membrane rather follows an end-over-end rotation. This solid-like motion is the tumbling movement. In Figure 12, we provide snapshots showing the TB motion in the first period and a biconcave shapes observed after several rotating periods. The evolution over time of the relative error in the global area and the perimeter is reported in Figure 13, showing good mass conservation which remains below 1% over several TB periods.

For this TB dynamics, we report the inclination angle θ_n of the vesicle and the corresponding adapted time steps in Figure 14. The results show higher values of the time step δt_n successfully adjusted when the membrane is close to a horizontal tilt characterized by a slow rotational dynamics due to the decrease of the external forces of the fluid. When the membrane is perpendicular to the flow, the fluid forces overcome the bending forces and generate rapid twist of the membrane. Following the fast movement, the adaptation strategy generates smaller time steps to better capture the dynamics. Overall, we observe a ratio factor of nearly 8 times between the smallest and largest time steps.

According to the analytic study in Keller and Skalak [2] (KS) and the experiments in Kantsler and Steinberg [90], there is a critical value of the ratio β, beyond which a vesicle initially following a TT motion, undergoes a transition from a TT to TB regime. Note that in 3D, a transitory regime, called trembling with trilobed membrane shapes, is additionally observed. To quantitatively validate our results, we proceed with a study of the TT-TB transition and report the critical viscosity contrast $\beta^\star$ necessary to observe this transition versus the reduced area Ξ_{2D}. We choose the parameters Re $= 10^{-3}$ and

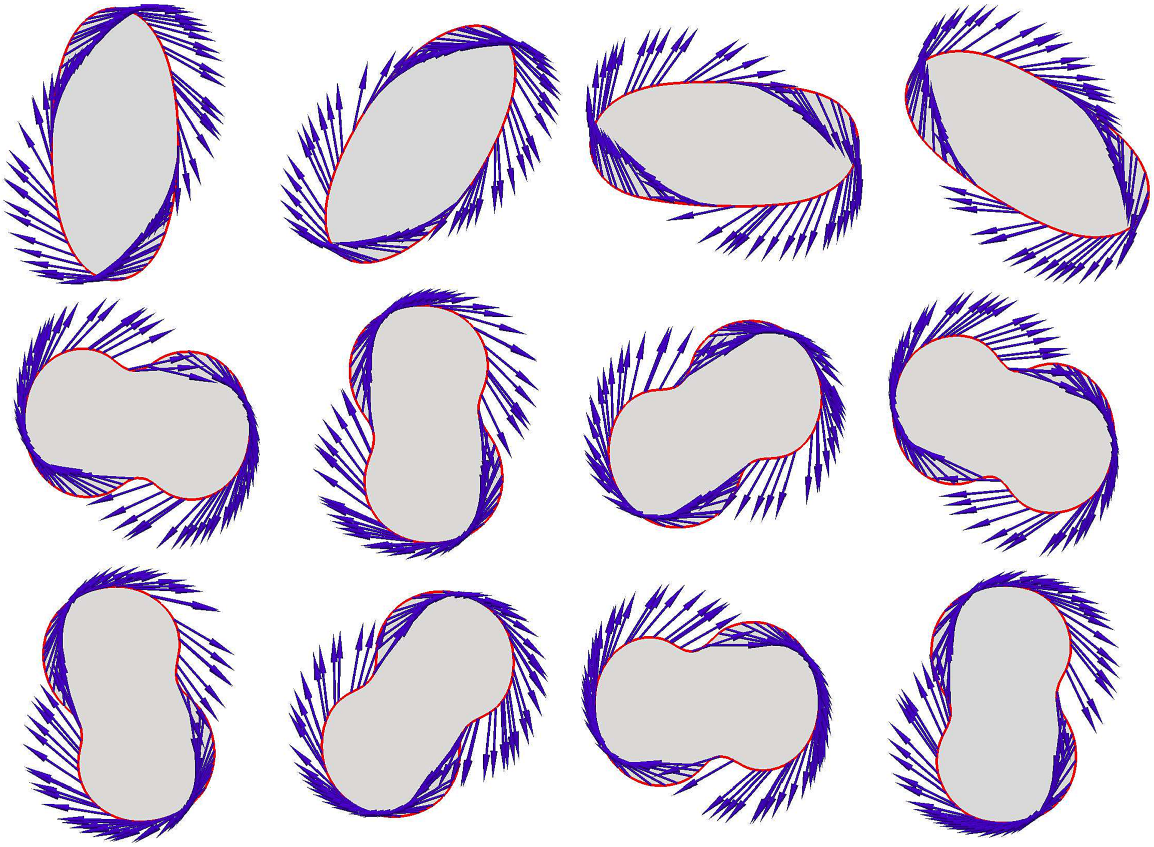

FIGURE 12 Example 3: Snapshots of a vesicle undergoing tumbling motion (TB) in simple shear flow. The snapshots show the deformations during the first and last periods at times $t \in \{0.83, 0.9, 1.2, 1.65, 11.17, 11.74, 12, 12.4, 12.8, 12.9, 13.1, 13.38\}$. [Colour figure can be viewed at wileyonlinelibrary.com]

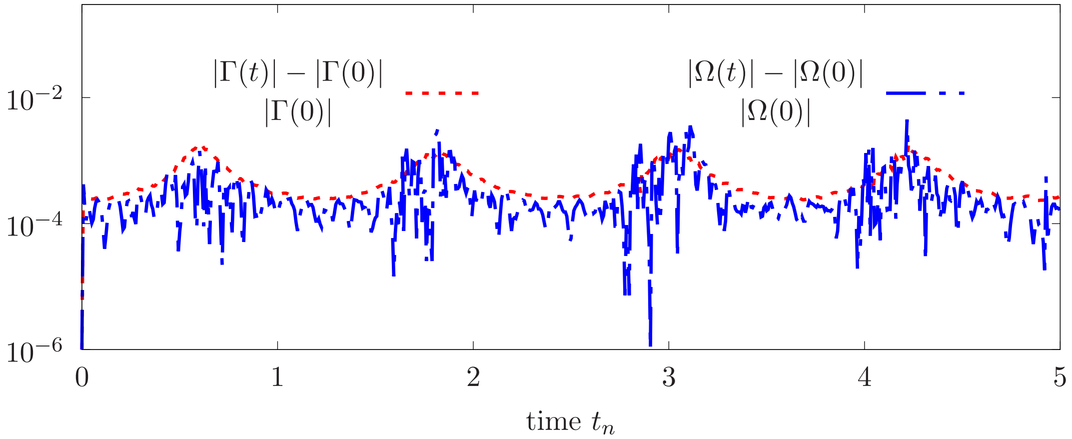

FIGURE 13 Example 3: Change over time of the relative area and relative perimeter of the vesicle under a tumbling motion, illustrating good mass conservation properties. [Colour figure can be viewed at wileyonlinelibrary.com]

$\mathrm{Bn} = 10^2$. For the Newtonian case obtained with $\varsigma = 1$, a correct behavior is observed. The phase diagram in Figure 15 shows good overall agreement with the the experimental study in Kantsler and Steinberg [90] and the numerical results using the phase field model [93] in the Stokes limit. Our results are slightly higher than those obtained with the level set method in Salac and Miksis [66] (with $\mathrm{Re} = 10^{-3}$ and $\mathrm{Bn} = 10^2$); This may be due to the penalty approach which does not allow to exactly fulfill the inextensibility constraint. Due to its simplifying assumptions, only a qualitative agreement is observed versus the 2D predictive theory of KS [2]. The later was obtained by assuming a fixed ellipsoidal shape of the vesicle, while only the flow orientation is allowed.

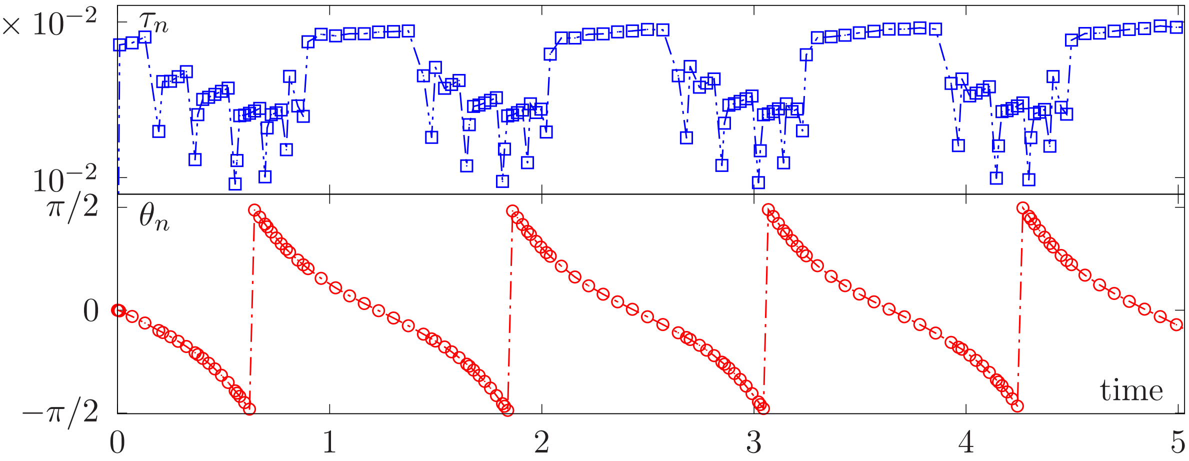

FIGURE 14 Example 3: Adapted time-step size δt_n and corresponding inclination angle an d θ_n when the fully periodic TB regime is established. Parameters of the simulation: Re = 10^{-2}, Bn = 10^3, and viscosity ratio is $\beta = 10$. [Colour figure can be viewed at wileyonlinelibrary.com]

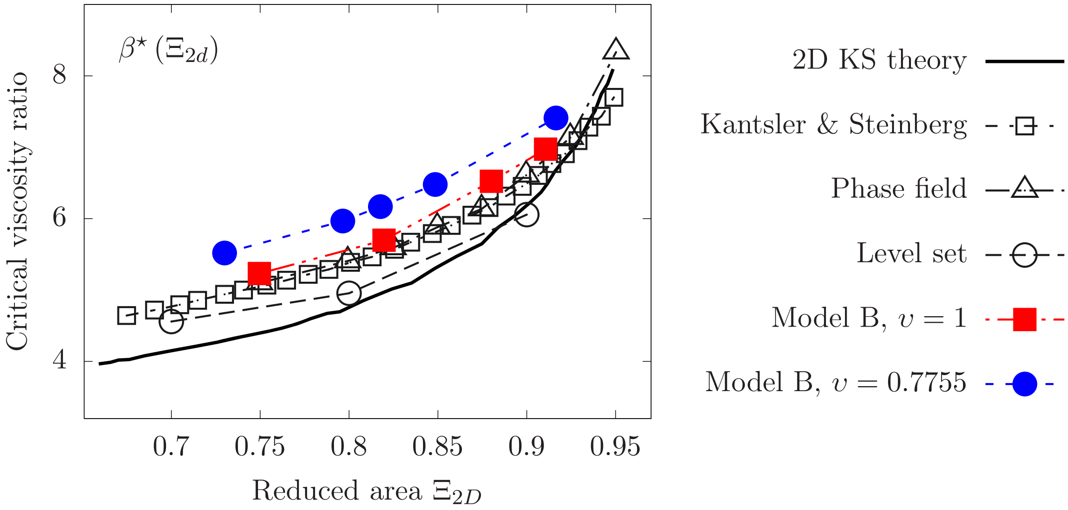

FIGURE 15 Example 3: State diagram showing the threshold viscosity contrast $\beta^\star$ as a function of the reduced area Ξ_{2D}. Comparison with the 2D KS theory [2], the experimental study of Kantsler and Steinberg [90], and the numerical results in Salac and Miksis [66] (level set and finite difference method) and Beaucourt et al. [93] (phase field and Stokes limit). [Colour figure can be viewed at wileyonlinelibrary.com]

7 | CONCLUSION

We have presented a finite element formulation for numerically simulating the dynamics of a single vesicle, mimicking a RBC, within a non-Newtonian fluid environment. In brief, the main contributions of this work can be summarized as follows: (i) The problem is formulated within a variational framework, employing a penalty approach that relaxes the local inextensibility constraint and facilitates a straightforward numerical implementation using standard generalized Stokes solvers commonly found in finite element software. (ii) For accurate calculations of geometric quantities and the highly nonlinear Helfrich force, which encompasses high derivatives of the level set function, we employ higher degree Lagrange polynomials in the spatial discretization. (iii) Moreover, we enhance the order of approximation in time by employing the double composition of discrete flow corresponding to the second-order Cranck–Nicolson integrator. (iv) We provide a theoretical error estimation, demonstrating that the double jump composition with complex coefficients achieves a higher fourth-order accuracy. Additionally, we offer a precise estimation of the numerical error up to $\mathcal{O}\left(\delta t^5\right)$ by utilizing the imaginary component. This estimation serves as a reliable criterion for adapting the time-step size. (v) We conducted a numerical study of the spatio-temporal convergence properties in stiff problems, showing the efficiency of the time-stepping strategy. Optimal convergence is achieved. (vi) Several numerical examples of the membrane dynamics, accompanied by quantitative comparisons, address in detail the relevance of the mathematical model in terms of physiological meaning. The influence of non-Newtonian rheology on the tilt angle of the TT regime and the phase diagram is investigated numerically. Accordingly, it becomes clear that a non-Newtonian realistic rheology has at least a quantitative impact on the dynamics of confined vesicles.

Further extensions of the presented methodology are being currently explored. Our primary focus is on the development of robust preconditioners that can significantly reduce the computational effort. This will enable us to more effectively explore the dynamics of membranes in non-Newtonian fluid environments in full three-dimensional settings. Furthermore, we foresee the development of error estimates in space as part of our future work.

ACKNOWLEDGEMENTS

The authors gratefully acknowledge the financial support by Khalifa University of Science and Technology through Grant FSU-2021-027 (#8474000367). The authors also wish to acknowledge the contribution of Khalifa University's research computing facilities to the results of this research.

CONFLICT OF INTEREST STATEMENT

The authors declare no potential conflict of interests.

ORCID

Aymen Laadhari https://orcid.org/0000-0002-8684-8293

REFERENCES

1. S. A. Safran, *Statistical thermodynamics of surfaces, interfaces and membranes*, Frontier in Physics, Vol. **90**, Addison-Wesley Publishing Company, Reading, Massachusetts, 1994.
2. S. R. Keller and R. Skalak, *Motion of a tank-treading ellipsoidal particle in a shear flow*, J. Fluid Mech. **120** (19827), 27–47.
3. T. Zhang and C. W. Wolgemuth, *A general computational framework for the dynamics of single- and multi-phase vesicles and membranes*, J. Comput. Phys. **450** (2022), 110815.
4. D. Salac and M. Miksis, *A level set projection model of lipid vesicles in general flows*, J. Comput. Phys. **230** (2011), no. 22, 8192–8215.
5. P. Connes, M. J. Simmonds, J. F. Brun, and O. K. Baskurt, *Exercise hemorheology: classical data, recent findings and unresolved issues*, Clin. Hemorheol. Microcirc. **53** (2013), no. 1–2, 187–99.
6. S. Karaz and E. Senses, *Liposomes under shear: structure, dynamics, and drug delivery applications*, Adv. NanoBiomed. Res. **3** (2003), no. 4, 2200101. https://onlinelibrary.wiley.com/doi/abs/10.1002/anbr.202200101
7. G. B. Thurston, *Rheological parameters for the viscosity viscoelasticity and thixotropy of blood*, Biorheology **16** (1979), no. 3, 149–162.
8. S. A. Wajihah and D. S. Sankar, *A review on non-Newtonian fluid models for multi-layered blood rheology in constricted arteries*, Arch. Appl. Mech. **93** (2023), no. 5, 1771–1796.
9. M.-C. Lai and Z. Li, *A remark on jump conditions for the three-dimensional Navier-Stokes equations involving an immersed moving membrane*, Appl. Math. Lett. **14** (2001), no. 2, 149–154.
10. A. Gizzi, R. Ruiz-Baier, S. Rossi, A. Laadhari, C. Cherubini, and S. Filippi, A three-dimensional continuum model of active contraction in single cardiomyocytes, *Modeling the heart and the circulatory system*, Springer International Publishing, Cham, 2015, pp. 157–176.
11. J. W. Barrett, H. Garcke, and R. Nurnberg, *Numerical computations of the dynamics of fluidic membranes and vesicles*, Phys. Rev. E **92** (2015), 52704.
12. T. Noyhouzer, C. L'Homme, I. Beaulieu, S. Mazurkiewicz, S. Kuss, H. B. Kraatz, S. Canesi, and J. Mauzeroll, *Ferrocene-modified phospholipid: an innovative precursor for redox-triggered drug delivery vesicles selective to cancer cells*, Langmuir **32** (2016), no. 17, 4169–4178.
13. B. Kaoui, *Computer simulations of drug release from a liposome into the bloodstream*, Europ. Phys. J. E **41** (2018), 1–6. https://link.springer.com/article/10.1140/epje/i2018-11626-7
14. Y. Elani, R. V. Law, and O. Ces, *Vesicle-based artificial cells as chemical microreactors with spatially segregated reaction pathways*, Nat. Commun. **5** (2014), 5305, DOI 10.1038/ncomms6305.
15. Y. Seol, Y.-H. Tseng, Y. Kim, and M.-C. Lai, *An immersed boundary method for simulating Newtonian vesicles in viscoelastic fluid*, J. Comput. Phys. **376** (2019), 1009–1027.
16. A. Laadhari and A. Deeb, *Computational modeling of individual red blood cell dynamics using discrete flow composition and adaptive time-stepping strategies*, Symmetry **15** (2023), no. 6, 1138, DOI 10.3390/sym15061138.
17. A. Laadhari, *Finite element method for the simulation of lipid vesicle / fluid interactions in a quasi-Newtonian fluid flow*, Math. **11** (2023), 1950, DOI 10.3390/math11081950.
18. W. Helfrich, *Elastic properties of lipid bilayers: theory and possible experiments*, Z. Naturforsch. C. **28** (1973), no. 11, 693–703.
19. P. B. Canham, *The minimum energy of bending as a possible explanation of the biconcave shape of the human red blood cell*, J. Theoret. Biol. **26** (1970), 61–81.

20. P. Bassereau, B. Sorre, and A. Lévy, *Bending lipid membranes: experiments after W. Helfrich's model*, Adv. Colloid Interface Sci. **208** (2014), 47–57. https://www.sciencedirect.com/science/article/pii/S0001868614000360. Special issue in honour of Wolfgang Helfrich.
21. O.-Y. Zhong-Can and W. Helfrich, *Bending energy of vesicle membranes: general expressions for the first, second, and third variation of the shape energy and applications to spheres and cylinders*, Phys. Rev. A **39** (1989), no. 10, 5280–5288.
22. A. Laadhari, C. Misbah, and P. Saramito, *On the equilibrium equation for a generalized biological membrane energy by using a shape optimization approach*, Phys. D **239** (2010), 1567–1572.
23. B. Kaoui, G. H. Ristow, I. Cantat, C. Misbah, and W. Zimmermann, *Lateral migration of a two-dimensional vesicle in unbounded Poiseuille flow*, Phys. Rev. E **77** (2008), 21903. https://link.aps.org/doi/10.1103/PhysRevE.77.021903
24. T. Zhang and C. W. Wolgemuth, *Sixth-order accurate schemes for reinitialization and extrapolation in the level set framework*, J. Scientif. Comput. **83** (2020), no. 2, 1–21.
25. C. Bui, V. Lleras, and O. Pantz, *Dynamics of red blood cells in 2d*, ESAIM Proc. **28** (2009), 182–194. http://www.esaim-proc.org/articles/proc/pdf/2009/03/proc092811.pdf
26. C. Pozrikidis, *Numerical simulation of the flow-induced deformation of red blood cells*, Ann. Biomed. Eng, **31** (2003), 1194–1205.
27. A. Rahimian, S. K. Veerapaneni, and G. Biros, *Dynamic simulation of locally inextensible vesicles suspended in an arbitrary two-dimensional domain, a boundary integral method*, J. Comput. Phys. **229** (2010), no. 18, 6466–6484.
28. B. Kaoui, J. Harting, and C. Misbah, *Two-dimensional vesicle dynamics under shear flow: effect of confinement*, Phys. Rev. E **83** (2011), 66319.
29. G.-H. Cottet, E. Maitre, and T. Milcent, *Eulerian formulation and Level-Set models for incompressible fluid-structure interaction*, Math. Model. Numer. Anal. **42** (2008), 471–492.
30. A. Laadhari, P. Saramito, and C. Misbah, *Computing the dynamics of biomembranes by combining conservative level set and adaptive finite element methods*, J. Comput. Phys. **263** (2014), 328–352.
31. A. Laadhari, *An operator splitting strategy for fluid-structure interaction problems with thin elastic structures in an incompressible Newtonian flow*, Appl. Math. Lett. **81** (2018), 35–43.
32. A. Laadhari and G. Szekely, *Fully implicit finite element method for the modeling of free surface flows with surface tension effect*, Int. J. Numer. Methods Eng. **111** (2017), no. 11, 1047–1074.
33. V. Doyeux, Y. Guyot, V. Chabannes, C. Prud'homme, and M. Ismail, *Simulation of two-fluid flows using a finite element/level set method. Application to bubbles and vesicle dynamics*, J. Comput. Appl. Math. **246** (2013), 251–59.
34. Q. Du, C. Liu, and X. Wang, *A phase field approach in the numerical study of the elastic bending energy for vesicle membranes*, J. Comput. Phys. **198** (2004), 450–468.
35. N. Valizadeh and T. Rabczuk, *Isogeometric analysis of hydrodynamics of vesicles using a monolithic phase-field approach*, Comput. Methods in Appl. Mech. Eng. **388** (2022), 114191. https://www.sciencedirect.com/science/article/pii/S0045782521005223
36. A. Bonito, R. H. Nochetto, and M. S. Pauletti, *Parametric FEM for geometric biomembranes*, J. Comput. Phys. **229** (2010), no. 9, 3171–3188. http://www.math.tamu.edu/~bonito/papers/2010_BonitoNochettoPauletti.pdf
37. W. R. Dodson and P. Dimitrakopoulos, *Oscillatory tank-treading motion of erythrocytes in shear flows*, Phys. Rev. E **84** (2011), 11913.
38. A. A. Joneidi, C. V. Verhoosel, and P. D. Anderson, *Isogeometric boundary integral analysis of drops and inextensible membranes in isoviscous flow*, Comput. Fluids **109** (2015), 49–66.
39. G. Boedec, M. Leonetti, and M. Jaeger, *Isogeometric FEM-BEM simulations of drop, capsule and vesicle dynamics in Stokes flow*, J. Comput. Phys. **342** (2017), 117–138. https://www.sciencedirect.com/science/article/pii/S0021999117302954
40. A. Laadhari, P. Saramito, C. Misbah, and G. Székely, *Fully implicit methodology for the dynamics of biomembranes and capillary interfaces by combining the level set and Newton methods*, J. Comput. Phys. **343** (2017), 271–299.
41. A. Laadhari, *Implicit finite element methodology for the numerical modeling of incompressible two-fluid flows with moving hyperelastic interface*, Appl. Math. Comput **333** (2018), 376–400.
42. A. Laadhari, *Exact Newton method with third-order convergence to model the dynamics of bubbles in incompressible flow*, Appl. Math. Lett. **69** (2017), 138–145.
43. G. W. Ernst Hairer, *Solving ordinary differential equations I: nonstiff problems*, 2nd ed., Springer Series in Computational Mathematics, Vol. **1**, Springer, Berlin, 2009.
44. C. F. Curtiss and J. O. Hirschfelder, *Integration of stiff equations*, Proc. Natl. Acad. Sci. U.S.A. **38** (1952), no. 3, 235–243.
45. H. J. Stetter, *Analysis of discretization methods for ordinary differential equations [by] Hans J. Stetter*, Springer, Berlin, New York, 1973.
46. A. Iserles, *Solving linear ordinary differential equations by exponentials of iterated commutators*, Numer. Math. **45** (1984), no. 2, 183–199.
47. M. Suzuki, *Fractal decomposition of exponential operators with applications to many-body theories and Monte Carlo simulations*, Phys. Lett. A **146** (1990), no. 6, 319–323. https://www.sciencedirect.com/science/article/pii/037596019090962N
48. H. Yoshida, *Construction of higher order symplectic integrators*, Phys. Lett. A **150** (1990), no. 5, 262–268.
49. E. Hairer and M. Hairer, *Frontiers in numerical analysis: Durham 2002*, Springer Berlin Heidelberg, Berlin, Heidelberg, 2003, pp. 199–240.
50. A. Deeb, D. Razafindralandy, and A. Hamdouni, *Comparison between Borel-Padé summation and factorial series, as time integration methods*, Discr. Contin. Dyn. Syst.- Ser. S **9** (2016), no. 2, 393–408.
51. D. Razafindralandy, V. Salnikov, A. Hamdouni, and A. Deeb, *Some robust integrators for large time dynamics*, Adv. Model. Simul. Eng. Sci. **6** (2019), no. 1, 5.
52. A. Deeb, A. Hamdouni, and D. Razafindralandy, *Performance of Borel-Padé-Laplace integrator for the solution of stiff and non-stiff problems*, Appl. Math. Comput **426** (2022), 127118.

53. A. Deeb, O. Kalaoun, and R. Belarbi, *Proper generalized decomposition using Taylor expansion for non-linear diffusion equations*, Math. Comput. Simul. **208** (2023), 71–94.
54. J. F. Nagle, M. S. Jablin, S. Tristram-Nagle, and K. Akabori, *What are the true values of the bending modulus of simple lipid bilayers?* Chem. Phys. Lipids **185** (2015), 3–10.
55. H. J. Deuling and W. Helfrich, *Red blood cell shapes as explained on the basis of curvature elasticity*, Biophys. J. **16** (1976), no. 8, 861–868.
56. G. Dziuk, *Computational parametric Willmore flow*, Numer. Math. **111** (2008), no. 1, 55–80.
57. F. Feng and W. S. Klug, *Finite element modeling of lipid bilayer membranes*, J. Comput. Phys. **220** (2006), no. 1, 394–408.
58. A. Laadhari, Y. Barral, and G. Székely, *A data-driven optimal control method for endoplasmic reticulum membrane compartmentalization in budding yeast cells*, Math. Methods Appl. Sci. **46** (2023), no. 8, 8855–8876.
59. B. Kaoui, G. Biros, and C. Misbah, *Why do red blood cells have asymmetric shapes even in a symmetric flow?* Phys. Rev. Lett. **103** (2009), 188101.
60. T. Metivet, A. Sengers, M. Ismail, and E. Maitre, *Diffusion-redistanciation schemes for 2D and 3D constrained Willmore flow: application to the equilibrium shapes of vesicles*, J. Comput. Phys. **436** (2021), 110288. https://www.sciencedirect.com/science/article/pii/S0021999121001832
61. S. Osher and J. A. Sethian, *Fronts propagating with curvature-dependent speed: algorithms based on Hamilton-Jacobi formulations*, J. Comput. Phys. **79** (1988), no. 1, 12–49.
62. M. Sussman and E. Fatemi, *An efficient, interface preserving level set re-distancing algorithm and its application to interfacial incompressible fluid flow*, SIAM J. Sci. Comput. **20** (1998), no. 4, 1165–1191.
63. A. Laadhari and G. Székely, *Eulerian finite element method for the numerical modeling of fluid dynamics of natural and pathological aortic valves*, J. Comput. Appl. Math. **319** (2016), 236–261.
64. J. Happel and H. Brenner, *Low Reynolds number hydrodynamics with special applications to particulate media*, Mechanics of Fluids and Transport Processes, Martinus Nijhoff Publishers, The Hague, Liège, 1983, DOI 10.1007/978-94-009-8352-6.
65. A. Laadhari, P. Saramito, and C. Misbah, *Vesicle tumbling inhibited by inertia*, Phys. Fluids **24** (2012), no. 3, 031901.
66. D. Salac and M. Miksis, *Reynolds number effects on lipid vesicles*, J. Fluid Mech. **711** (2012), 122–146.
67. F. Brezzi and M. Fortin, *Mixed and hybrid finite element methods*, Springer, New York, 1991.
68. J. Janela, A. Lefebvre, and B. Maury, *A penalty method for the simulation of fluid–rigid body interaction*, ESAIM: Proc. **14** (2005), 115–123, DOI 10.1051/proc:2005010.
69. R. A. Adams and J. J. F. Fournier, *Sobolev spaces*, 2nd ed., Elsevier,, Amsterdam 2003.
70. S. C. Brenner and L. R. Scott, *The mathematical theory of finite element methods*, 3rd ed., Springer, New York, 2008.
71. A. N. Brooks and T. J. R. Hughes, *Streamline upwind/Petrov-Galerkin formulations for convection dominated flows with particular emphasis on the incompressible Navier-Stokes equations*, Comput. Methods in Appl. Mech. Eng. **32** (1982), no. 1, 199–259.
72. T. J. R. Hughes, L. P. Franca, and G. M. Hulbert, *A new finite element formulation for computational fluid dynamics: VIII. The Galerkin/least-squares method for advective-diffusive equations*, Comput. Methods Appl. Mech. Eng. **73** (1989), no. 2, 173–189. https://www.sciencedirect.com/science/article/pii/0045782589901114
73. R. Codina, *Comparison of some finite element methods for solving the diffusion-convection-reaction equation*, Comput. Methods in Appl. Mech. Eng. **156** (1998), no. 1, 185–210. https://www.sciencedirect.com/science/article/pii/S0045782597002065
74. E. Loch. (2013). *The level set method for capturing interfaces with applications in two-phase flow problems*, Ph.D. Thesis, Publikationsserver der RWTH Aachen University, Aachen. https://publications.rwth-aachen.de/record/229393. Zsfassung in dt. und engl. Sprache; Aachen, Techn. Hochsch., Diss., 2013.
75. E. Hairer, C. Lubich, and G. Wanner, *Geometric numerical integration: structure-preserving algorithms for ordinary differential equations*, Springer Series in Computational Mathematics, Springer, 2002.
76. F. Casas, P. Chartier, A. Escorihuela-Tomàs, and Y. Zhang, *Compositions of pseudo-symmetric integrators with complex coefficients for the numerical integration of differential equations*, J. Comput. Appl. Math. **381** (2021), 113006.
77. F. Castella, P. Chartier, S. Descombes, and G. Vilmart, *Splitting methods with complex times for parabolic equations*, Bit Numer. Math. **49** (2009), 487–508.
78. E. T. Whittaker and G. N. Watson, *A course in modern analysis*, 5th ed., Cambridge University Press, Cambridge, England, 1990, pp. 96–98.
79. Z. Zhang and Z. Qiao, *An adaptive time-stepping strategy for the Cahn-Hilliard equation*, Commun. Comput. Phys. **11** (2012), no. 4, 1261–1278.
80. S. Guo and J. Ren, *A novel adaptive Crank-Nicolson-type scheme for the time fractional Allen-Cahn model*, Appl. Math. Lett. **129** (2022), 107943. https://www.sciencedirect.com/science/article/pii/S0893965922000246
81. J.-J. Xu, Z. Li, J. Lowengrub, and H. Zhao, *A level-set method for interfacial flows with surfactant*, J. Comput. Phys. **212** (2006), no. 2, 590–616.
82. L. Ma and W. S. Klug, *Viscous regularization and r-adaptive remeshing for finite element analysis of lipid membrane mechanics*, J. Comput. Phys. **227** (2008), no. 11, 5816–5835.
83. M. S. Alnaes, J. Blechta, J. Hake, A. Johansson, B. Kehlet, A. Logg, C. Richardson, J. Ring, M. E. Rognes and G. N. Wells, *The FEniCS project version 1.5*, Arch. Numer. Softw. **3** (2015), no. 100, 9–93.
84. P. Saramito, *Efficient C++ finite element computing with Rheolef*, CNRS-CCSD, Grenoble, France, 2020. https://packages.debian.org/unstable/rheolef. HAL version: v15. Accessed: 12.03.23.

85. U. Ayachit, A. Bauer, B. Geveci, P. O'Leary, K. Moreland, N. Fabian and J. Mauldin, *ParaView Catalyst: enabling in situ data analysis and visualization*, Proceedings of the First Workshop on In Situ Infrastructures for Enabling Extreme-Scale Analysis and Visualization, ISAV2015, Association for Computing Machinery, New York, NY, USA, 2015, pp. 25–29.
86. P. K. Janert, *Gnuplot in action, understanding data with graphs*, 2nd ed., Manning, Greenwich, 2011.
87. J. B. Bell, P. Colella, and H. M. Glaz, *A second-order projection method for the incompressible Navier-Stokes equations*, J. Comput. Phys. **85** (1989), no. 2, 257–283. https://www.sciencedirect.com/science/article/pii/0021999189901514
88. R. J. LeVeque, *High-resolution conservative algorithms for advection in incompressible flow*, SIAM J. Numer. Anal. **33** (1996), no. 2, 627–665.
89. M. Kraus, W. Wintz, U. Seifert, and R. Lipowsky, *Fluid vesicles in shear flow*, Phys. Rev. Lett. **77** (1996), 3685.
90. V. Kantsler and V. Steinberg, *Transition to tumbling and two regimes of tumbling motion of a vesicle in shear flow*, Phys. Rev. Lett. **96** (2006), 36001. https://link.aps.org/doi/10.1103/PhysRevLett.96.036001
91. B. Kaoui and J. Harting, *Two-dimensional lattice Boltzmann simulations of vesicles with viscosity contrast*, Rheolog. Acta **55** (2016), 465–475. https://link.springer.com/article/10.1007/s00397-015-0867-6
92. T. M. Fischer, M. Stöhr-Liesen, and H. Schmid-Schönbein, *The red cell as a fluid droplet: tank tread-like motion of the human erythrocyte membrane in shear flow*, Science **202** (1978), no. 4370, 894–896.
93. J. Beaucourt, F. Rioual, T. Séon, T. Biben, and C. Misbah, *Steady to unsteady dynamics of a vesicle in a flow*, Phys. Rev. E **69** (2004), 11906.

How to cite this article: A. Laadhari, A. Deeb, and B. Kaoui, *Hydrodynamics simulation of red blood cells: Employing a penalty method with double jump composition of lower order time integrator*, Math. Meth. Appl. Sci. (2023), 1–27, DOI 10.1002/mma.9607.